

Overview of observations from the RADAGAST experiment in Niamey, Niger.

Part 2: Radiative fluxes and divergences

A. Slingo, H. E. White, N. A. Bharmal and G. J. Robinson

Environmental Systems Science Centre, University of Reading, UK

8 May 2008

Abstract

Broadband shortwave and longwave radiative fluxes observed both at the surface and from space during the RADAGAST experiment in Niamey, Niger in 2006 are presented. The surface fluxes were measured by the Atmospheric Radiation Measurement (ARM) Program Mobile Facility (AMF) at Niamey airport, while the fluxes at the top of the atmosphere (TOA) are from the Geostationary Earth Radiation Budget (GERB) instrument on the Meteosat-8 satellite. The data are analyzed as daily averages, in order to minimise sampling differences between the surface and top of atmosphere instruments, while retaining the synoptic and seasonal changes that are the main focus of this study. The fluxes are combined to provide estimates of the divergence of radiation across the atmosphere throughout 2006.

The influence of temperature, water vapor, aerosols and clouds on the fluxes and divergences is investigated. Simple models are used to interpret these results and to place them in the context of previous studies. Aerosols are ubiquitous throughout the year and have a significant impact on both the shortwave and longwave fluxes. The large and systematic seasonal changes in temperature and column integrated water vapor (CWV) through the dry and wet seasons are found to exert strong influences on the longwave fluxes and on the atmospheric divergence. These influences are often in opposition to each other, because the highest temperatures occur at the end of the dry season when the CWV is lowest, while in the wet season the lowest temperatures are associated with the highest values of CWV.

The atmospheric longwave divergence is remarkably constant through the year,

because of a compensation between the seasonal variations in the outgoing longwave radiation (OLR) and surface net longwave radiation. A simple model of the greenhouse effect is used to interpret this result in terms of the dependence of the normalized greenhouse effect at the TOA and of the effective emissivity of the atmosphere at the surface on the CWV. It is shown that, as the CWV increases, the atmosphere loses longwave energy to the surface with about the same increasing efficiency with which it traps the OLR, thus keeping the atmospheric longwave divergence roughly constant.

These results show that the meteorology of the West African monsoon leads to a radiative environment that is radically different from that in other climatic regions.

1. Introduction

Radiative processes are of crucial importance in determining the basic characteristics of the climate system, its stability and its response to perturbations. Understanding the radiation budget and what controls it is central to climate science, because changes in the budget are driving climate change and are also involved in the associated feedbacks (Randall et al. 2007). In recent decades, satellite observations have provided an accurate description of the radiation budget at the top of the atmosphere (TOA) and its seasonal and interannual variability (Wong et al. 2006, Loeb et al. 2007). In contrast, the radiation budget at the surface is less well observed, because almost all of the long-term observing sites are over land and their spatial distribution is very heterogeneous (Ohmura et al. 1998). Retrievals of the surface radiation budget over the whole globe are now available from satellite data, using additional datasets and modelling, which have been validated against the surface sites (Zhang et al. 2004, Stackhouse et al. 2004). Nevertheless, estimates of the divergence of radiation across the atmosphere, obtained by differencing the radiation budget at the surface from that at the TOA, show significant variations depending on the datasets employed. For example, estimates of the global and annual mean shortwave (solar) radiation absorbed by the atmosphere vary from 67 to 93 Wm^{-2} (Kiehl and Trenberth 1997, Ramana et al. 2007).

One approach to making progress in characterizing the atmospheric divergence and in understanding what controls it is to combine radiative fluxes and other measurements from a

single, well-instrumented surface site with satellite data. Unfortunately, until recently, all broad-band satellite radiometers have flown in low Earth orbits, so the availability of data over a given surface site has been limited in its temporal resolution and diurnal coverage. This situation improved dramatically with the launch of the first Geostationary Earth Radiation Budget (GERB) instrument on the Meteosat-8 European weather satellite in August 2002 (Harries et al. 2005). GERB provides broad-band shortwave and longwave fluxes every 15 minutes at about 50km resolution within the Meteosat field of view. Building on this advance, a proposal was submitted to the U.S. Department of Energy's Atmospheric Radiation Measurement (ARM) Program to deploy their new ARM Mobile Facility (AMF) to Niamey, the capital of Niger in West Africa, to make coordinated measurements with GERB in collaboration with the African Monsoon Multidisciplinary Analysis (AMMA) experiment (Redelsperger et al. 2006), the field phases of which were due to take place in 2006. This proposal was called RADAGAST (Radiative Atmospheric Divergence using ARM Mobile Facility, GERB data and AMMA stations). Further details on the background to the AMF and its deployment to Niger for the RADAGAST experiment are provided by Miller and Slingo (2007).

The African continent provides a unique environment within which to study the physical processes that control the radiation budget. North Africa is the most important source of wind-blown dust in the world (Prospero et al. 2002) and the burning of vegetation in the dry seasons to clear the ground for crops can lead to high loadings of biomass aerosols. The extended drought that occurred in the Sahel in the 1970s and 1980s (Bell and Lamb 2006) stimulated extensive research to discover the cause, which included the suggestion that radiative and biogeophysical feedbacks could be involved (Charney 1975). The climate of the Sahel is strongly influenced by the West African monsoon, which regulates the seasonal cycle of dry and wet seasons in response to the changing solar forcing. This important system was the focus of the AMMA observations in 2006. In association with AMMA, several focused experiments studied various aspects of the monsoon. In particular, the DABEX experiment built on previous airborne campaigns to make *in situ* measurements of the radiative properties of wind-blown dust and of aerosols from biomass burning in the dry season (Haywood et al. 2008).

An overview of the RADAGAST observations of the meteorology and thermodynamic variables is provided in a companion paper (Slingo et al. 2008; hereafter Part 1). Here, the focus is on the radiative fluxes both at the top of the atmosphere (TOA) and at the surface, and on the first direct

estimates of the divergence of radiation across the atmosphere. The surface fluxes were measured by the AMF at the main Niamey airport site (13° 29'N, 2° 10'E). The TOA fluxes were measured by the GERB broadband radiometer on Meteosat-8, stationed above 0° longitude.

In contrast to previous field studies that have invariably been of short duration, this paper presents the radiative fluxes and derived divergences for the whole of 2006, and investigates the influences of controlling factors such as temperature, water vapor, clouds and aerosols. These results are the first estimates of broadband radiative divergences using both surface and satellite observations that are available both at high temporal resolution and for such an extended period of time. The philosophy of the approach taken in the analysis is to use the minimum of detailed radiative transfer modelling, since this is the remit of some of the following papers in this special section. Rather, the emphasis is on presenting the timeseries of the various radiative quantities and to use scatter plots, simple models and to a limited degree the results from the other studies to identify the main factors that control the fluxes and divergences.

Many difficult sampling issues arise when bringing together measurements from the surface and from space to calculate atmospheric flux divergences above a single location (Settle et al. 2008). We minimize these issues in this first study of the divergences from RADAGAST by using daily averaged data and by analyzing only the divergences across the atmosphere as a whole, as opposed to the vertical structure of the divergences within the atmosphere. As a result, the effects of residual sampling uncertainties and of errors in the calibration of the instruments are much smaller than the magnitude of the divergences themselves, so they have a much less damaging impact on the analysis than would be the case for data with higher time and space resolution.

In the following section, the data used and the processing are described. Section 3 presents timeseries of cloud and aerosol retrievals that are used later to investigate their influence on the fluxes and divergences. Timeseries of the radiative fluxes from the AMF at the surface and from GERB at the TOA are analyzed in Section 4. Scatter plots are used in Section 5 to investigate the relative roles of temperature, water vapor, clouds and aerosols on the fluxes. The derived divergences are presented in Section 6, both as timeseries and as scatter plots, which are used to explore the factors that control the divergences. The longwave fluxes and divergences are analysed further in Section 7 using a simple model of the greenhouse effect. Finally, Section 8 summarises and discusses the main results of this work.

2. Data sources, processing and errors

2.1. Radiative fluxes

Upwelling and downwelling longwave (thermal) and shortwave (solar) radiative fluxes measured at the surface were obtained from the radiometers at the main Niamey airport site. Details of the AMF instruments and of their characteristics are given by Miller and Slingo (2007). The total downwelling shortwave radiation was calculated using the component sum method (McFarlane et al. 2008), whereby the direct flux measured normal to the direction of the sun is multiplied by the cosine of the solar zenith angle and added to the measured diffuse flux. This provides a more accurate estimate of the total downwelling flux than a measurement of the sum of the direct and diffuse fluxes by a single radiometer.

Outgoing longwave radiation (OLR) and reflected shortwave radiation at the TOA were obtained from the GERB instrument on Meteosat-8 (Harries et al. 2005). Version 3 ARG data from GERB were retrieved from the Royal Meteorological Institute of Belgium, in near real-time with a latency of about 40 minutes. The ARG data were replaced by quality-controlled Edition 1 data produced by the GERB Ground Segment Processing System after about 40 days (Harries et al. 2005, Dewitte et al. 2008). The GERB instrument was turned off for periods of several hours or longer on 16 individual days in 2006 and for a longer period from 24 September to 9 October, because of autonomous or commanded safety shutdowns. In addition, the instrument was routinely shut down for up to 6 hours around midnight during the eclipse seasons at the equinoxes, to prevent direct sunlight from damaging the detectors (Harries et al. 2005). In 2006, these periods covered 9 February to 23 April and 18 August to 30 October.

All of the radiative fluxes shown here are daily means, which simplifies combining the ARM point measurements with the GERB area-average measurements. The averaging process removes the diurnal variability and the high frequency noise that arises from small-scale cloud features advecting over the AMF and through the GERB pixels. It also simplifies investigations of the influence of the meteorological changes on the fluxes and divergences over a timescale of days and longer, which is the primary focus of this work.

2.2. Sources of error in the radiative fluxes and divergences

The errors in the daily mean fluxes and divergences arise from three main sources, which are considered below. Combining these sources enables an estimate of the overall error to be made.

2.2.1. AMF and GERB fluxes

This source of error includes the instruments themselves and the processing of the measurements to produce fluxes. Uncertainties in the AMF fluxes are given by Slingo et al. (2006) as 9.0 Wm^{-2} for the total downwelling shortwave, although this could be as large as 25 Wm^{-2} at the peak of the March 2006 dust storm, and 5.1 Wm^{-2} for the downwelling longwave. Estimates of the absolute accuracy of the GERB radiances are given by Slingo et al. (2006) as 2.25% in the shortwave and 0.96% in the longwave. They note that angular models introduce additional errors of 10 Wm^{-2} for typical shortwave fluxes and 5 Wm^{-2} for longwave fluxes, with the expectation that the latter will be an underestimate for aerosols, which are not (as yet) identified in the processing system. Results shown by Bharmal et al. (2008) are consistent with this conclusion. Dewitte et al. (2008) analyse comparisons between co-located GERB and CERES data and conclude that the GERB accuracy is 5% for reflected shortwave radiances and 2% for the emitted longwave radiances. For typical daily mean shortwave and longwave fluxes shown later of $100\text{--}200 \text{ Wm}^{-2}$ and 300 Wm^{-2} , respectively, these numbers correspond to $5\text{--}10 \text{ Wm}^{-2}$ and 6 Wm^{-2} , consistent with the estimates from Slingo et al. (2006) quoted above.

2.2.2. Interpolation across missing data

The most serious source of missing data for the daily means is the shutdown of GERB during the eclipse seasons, with the loss of up to 6 hours of data every night. Shortwave data are also masked as unavailable during the sun-glint period of about one hour around 1130 local time. A simple linear interpolation of the data across these periods was applied. The impact was quantified by applying the interpolation to days when data were present and comparing the actual and interpolated daily means. For the interpolation at night, the impact on the OLR was $-0.1 \pm 0.8 \text{ Wm}^{-2}$ for clear days and $0.1 \pm 2.5 \text{ Wm}^{-2}$ for cloudy days. The small systematic component reflects the fact that the OLR typically changes quite slowly through the night, at least for clear skies, and this behavior is approximately linear (e.g. Comer et al. 2007). For the shortwave interpolation, the impact on the reflected shortwave was $-5 \pm 5 \text{ Wm}^{-2}$ for clear days and $-4 \pm 17 \text{ Wm}^{-2}$ for cloudy days. Extended periods during which GERB was turned off for other reasons could not be dealt with in this way (notably 24 September to 9 October), so these days were excluded from the analysis altogether.

2.2.3. Inhomogeneities and spatial sampling

Spatial sampling issues (quote results from Settle et al. 2008). The results from the end of Bharmal et al. (2008) also provide an independent estimate of the compatibility of the GERB and AMF data. **TBC**.

2.2.4. Estimate of the errors in the divergences

Make the usual assumption that the above terms are uncorrelated, to produce an overall error estimate for the divergences. These will be bigger than the 15 Wm^{-2} shortwave and 7 Wm^{-2} longwave values stated or implied by Slingo et al. (2006), but perhaps not much bigger. **TBC**.

2.3. Clouds

Two complementary cloud masks were used in the analysis of the fluxes. The first is based on the operational CLMK cloud mask product generated by the Nowcasting Software Application Facility using SEVIRI (Spinning Enhanced Visible and Infrared Imager) data on Meteosat-8 (Schmetz et al. 2002). This is available throughout the period from the EUMETSAT on-line archive (archive.eumetsat.org). The CLMK data are at the same spatial and temporal resolution as the SEVIRI imagery (3km and 15 minutes). They are derived from a higher-level cloud classification product, which uses a two step process to first identify clouds, and then classify them (Derrien and Gléau, 2005). The cloud identification and classification processes both use a series of tests based on multi-spectral thresholds, where the threshold values are determined dynamically depending on illumination conditions and geographical location, climatological data, numerical weather prediction data and radiative transfer models. At night time only those tests that use the thermal infrared SEVIRI channels are available, with the result that the cloud classification is less reliable: for example, airborne dust is sometimes indistinguishable from low warm clouds. For the AMF Niamey airport and Banizoumbou sites, regions of 17 by 17 pixels (corresponding to a GERB ARG pixel) centred on each site were extracted from the CLMK data, from which time series of top-of atmosphere estimates of cloud cover were generated.

The second cloud mask was derived from the cloud fractions retrieved by Kollias et al. (2008) from the W-band (95GHz) cloud radar, micropulse Lidar and ceilometer at the main AMF airport site. Unfortunately, these do not cover the entire year, because the cloud radar only became operational in mid-April. Daily mean cloud fractions were calculated as vertical means of the daily mean values at all levels from Kollias et al. (2008). This provides a simple indication of the cloud amount present each day, rather than an estimate of average cloud optical thickness or sky

cover, since this method clearly does not distinguish between days with thin cloud throughout the atmosphere from days with thick clouds at only a few levels. This was done as a simple means of producing a binary cloud mask for the radiation data, days having a mean cloud fraction of more than 0.05 being classed as ‘cloudy’.

2.4. Aerosols

Retrievals of aerosol optical thickness were obtained from the AERONET site at Banizoumbou, approximately 60km east of Niamey airport (Holben et al. 2001). The data from this site represent the most comprehensive and local retrievals that are available throughout the AMF deployment. A CIMEL sunphotometer, as used by AERONET, was also deployed at the AMF Niamey airport site, but was only present from August 2006 until the end of the deployment, so the Banizoumbou data are preferred here. The data used are the diurnally-averaged AERONET version 2 direct sun inversions of aerosol optical thickness at 870nm. These data have the advantage of being cloud screened with associated error estimates; the so-called Triplet Variance, from 3 measurements within 90 seconds. Turner (2008) uses these AERONET data to compare with optical thicknesses retrieved from the AERI infra-red window radiances and confirms that the data correlate well with the infra-red optical thicknesses.

3. Cloud and aerosol timeseries

In this and the subsequent sections, the wet season is defined as in Part 1; from 5 May to 29 October. The period before 5 May is referred to as the first dry season and that after 29 October as the second dry season.

3.1. Clouds

Figure 1a shows the mean cloud fractions derived from the SEVIRI data as the solid line. In the first dry season, cloud amounts were low, with mainly thin cirrus associated with the sub-tropical jet stream to the north or with convection to the south of Niamey, plus occasional thin mid-level clouds that formed at the top of the aerosol-laden boundary layer at around 5km altitude. Cloud amounts increased with the arrival of the wet season and most cloud occurred in July, August and September, associated with the summer monsoon. The early and late monsoon periods were relatively clear in comparison, probably due to the moist monsoon air layer being too shallow to

support deep convection, although the onset and retreat of the monsoon were still apparent in the change in the amount and frequency of cloud. The summer monsoon brought in the moisture necessary to support deep, moist convection, and so summer cloud types were more variable, consisting not only of thin cirrus, but also thicker low and mid-level convective cloud. Following the retreat of the monsoon in October, cloud amounts returned to small amounts of cirrus.

The dashed line on Figure 1a shows the cloud fractions derived from the Kollias et al. (2008) data. These correlate well with the SEVIRI data, although the absolute amounts of cloud are not the same, because of differences between the fields of view of the satellite and AMF instruments and between the cloud detection algorithms. It was found that the results shown later were not sensitive to which cloud mask was used to sample the data for clear and cloudy conditions. Given that the SEVIRI mask is available for the entire year, it was therefore decided to use this exclusively in the results shown in this paper.

3.2. Aerosols

Aerosol loadings were significant throughout the year (Figure 1b), with several major events in addition to the previously documented dust storm in early March (Slingo et al. 2006). Apart from these individual dust outbreaks, the background aerosol optical thickness remained at around 0.3 for the first half of the year, falling gradually during the late summer monsoon period to around 0.2, and reaching the lowest levels during the second dry season. The largest sustained values were in the wet season, particularly in June, when dust was raised by the gust fronts propagating away from deep convection. The reduction in background levels late in the monsoon may have been due to the wetting of the surface and the growth of vegetation following rainfall, both of which would have reduced the amount of dust available to be lifted by the wind. The lowest aerosol loadings occurred in the second dry season, providing good conditions for testing clear-sky radiation simulations (Bharmal et al. 2008).

4. Radiative flux timeseries

This section presents the radiative fluxes measured at the surface by the AMF and at the TOA by GERB. The fluxes are presented first as time series to show the variation over the course of the year, and are then shown plotted against the dominant influences on this variability to illustrate the main controls on the radiation fields. Understanding the controls on the radiative fluxes is

essential for interpreting the radiative divergence results, to be discussed in section 6, as the divergences are calculated from the component fluxes.

4.1. Surface longwave fluxes

Figure 2 shows the surface downwelling, upwelling and net longwave radiative fluxes measured by the AMF at Niamey airport. Downwelling longwave radiation (DLR, Figure 2a) increased overall through the first dry season by about 30 Wm^{-2} , but periodic increases above the base level of over 50 Wm^{-2} occurred during this period, coinciding with dry season cloud and water vapour advection events, as well as the dust storm in early March. The onset of the monsoon can be seen clearly in mid April, when the DLR showed a sudden increase with the arrival of more humid air. This was referred to as a “false onset” in Part 1, as it was followed by a break, the main monsoon arriving only at the beginning of May. The DLR reached a maximum during the early part of the wet season, when the atmosphere was still relatively cloud free (Figure 1a), but very warm and humid. It then dropped by over 20 Wm^{-2} in the later and cloudier part of the monsoon, when the increased cloud cover and hence lower shortwave insolation (see below), coupled with greater evaporation from the surface, led to lower surface and atmospheric temperatures. The end of the monsoon at the end of October was associated with a precipitate drop in the column water vapor, CWV (Part 1, Figure 8), which produced a corresponding reduction in the DLR of over 50 Wm^{-2} . In the second dry season, the strong signals from variations in CWV and in aerosol loadings (Figure 1b) are once again apparent. The lowest fluxes occurred at the end of the year, when the surface and air temperatures reached their minimum values (Part 1).

While the behavior of the downward thermal fluxes described above appears straightforward, it actually results from a very unusual combination of changes in temperature and humidity. As shown in Part 1, surface and air temperatures increased during the first dry season to a maximum at the start of the monsoon in May. Temperatures then decreased to the peak of the monsoon in August, recovered in September/October, before dropping steadily towards the end of the year. In contrast, near-surface humidities and the CWV decreased through the first dry season, then increased as the monsoon arrived and reached their highest values at the peak of the monsoon. They decreased in September/October and dropped to low values again at the end of the year. Apart from in the second dry season, the seasonal changes in temperature and humidity were thus in antiphase to each other. The reason is that humidity variations in this region are controlled by

the wind direction and by the origin of the airmass (and hence by the large-scale atmospheric dynamics) more than by the temperature. This aspect of the climatology of the region is well known, but the impact on the longwave radiative fluxes and divergences is remarkable, as discussed later. As far as we are aware, this behavior has not been documented before.

The upwelling longwave radiation (Figure 2b) is determined by the surface temperature and emissivity, with changes in the latter being less important (Settle et al. 2008). The surface temperature was in general slightly higher than the air temperature, but the two were closely coupled, so that comparison of Figure 2b with the timeseries of air temperature (Figure 5, Part 1) shows that both the low and high frequency variations in the upward flux closely followed those of the temperature.

The net longwave radiation at the surface (Figure 2c) is also dependent on temperature, as is shown later, but the most consistent influence appears to be from the CWV, as may be seen by comparing with Figure 8 in Part 1. The largest net longwave thus occurred at the end of the first dry season, when the CWV was at its lowest value, which allowed the surface to cool most efficiently out to space. The net longwave dropped progressively through the wet season, reaching a minimum in August when the CWV reached its maximum. At this time, the atmosphere was at its most opaque and so the surface cooling was minimised. The net longwave increased again during the second dry season, as the CWV fell again. Cloud events always reduced the net longwave, particularly so during the dry seasons when the low CWV led to values of the cloud radiative effect that reached several tens of Wm^{-2} , even from the middle level and high clouds present at this time.

4.2. Surface shortwave fluxes

The incoming shortwave radiation (Figure 3a) increased with the seasonal increase in insolation at the TOA through the first dry season until near the end of April, when the sun passed overhead at Niamey (Figure 4c). During the monsoon, solar radiation received at the surface decreased substantially, mainly because of the increased cloudiness but also, as will be shown later, because of water vapor absorption. The incoming shortwave was thus lower when the sun passed overhead for the second time in late August, compared with April, and continued to decrease thereafter as the sun moved further south. Comparison with Figure 1 shows that both clouds and aerosol caused large reductions all year round from the clear sky values, but that these became

more frequent in the wet season, particularly during the cloud maximum between July and September. The impact of the dust storms evident in Figure 1b, such as that in early March and the extended feature in mid-June, can also be seen clearly. These are the main causes of reduced solar transmission to the surface during the dry season, apart from the impact of two cloud events during the first dry season. The onset and retreat of the monsoon were not so clearly marked in the solar than in the thermal, and the retreat appeared to occur almost a month sooner. This is because the main effect of the monsoon on solar fluxes is the impact of cloud, with a smaller impact of humidity. In the thermal region, the humidity of the monsoon air layer is much more important. The build up of monsoon cloud happened gradually, whereas the arrival of the monsoon air brings a sudden change in water vapour content. In addition, the area of convection moves south sooner than the moist air layer since it becomes shallower towards the north, therefore becoming too shallow to support cloud late in the monsoon season.

Reflected shortwave radiation (Figure 3b) shows the same basic pattern, with the additional effect of changes in the surface albedo (McFarlane et al. 2008). The reduction in albedo during the wet season due to the higher average sun angle and the darkening of the surface due to rainfall and vegetation growth reduced the reflection at this time, amplifying the seasonal changes seen in the incoming shortwave.

The net shortwave (Figure 3c) shows that the absorption of solar radiation by the surface was a maximum in the early period of the wet season, but was reduced substantially by cloud from July through September. This reduction in the insolation drove the drop in surface and air temperatures through the monsoon, documented in Part 1. The signals of dust events and of cloud at all times of the year, apparent in the component fluxes, can also be seen in the net radiation.

4.3. Top of atmosphere fluxes measured by GERB

Figure 4a shows that the OLR increased during the first dry season and then dropped by over 50 Wm^{-2} as the monsoon developed, recovering during the second dry season. These changes were driven in part by the same temperature and CWV variations discussed above, but in the case of the OLR these variations mostly acted in the same direction, so that OLR increased both because of increasing temperature and of decreasing CWV during the first dry season, and similarly decreased in the wet season as the CWV increased and the surface and lower tropospheric temperatures fell. This picture is complicated by clouds and to a lesser extent aerosol outbreaks,

both of which acted to reduce the OLR. The cloud effect is apparent throughout the year, although the deep convective cloudiness during the monsoon consistently produced the lowest OLR values. Following the monsoon retreat, OLR rose as the atmosphere again became more transparent to thermal radiation. Towards the end of the year, several exceptionally clear and dry periods allowed the OLR to rise, countering the effect of the fall in surface temperature.

The annual variation in the reflected solar radiation at the TOA (Figure 4b) is controlled by the insolation (Figure 4c), which was a minimum at the beginning of the year when the sun was furthest south and a maximum when the sun passed overhead in late April. The main cause of short-term albedo increases was the presence of bright, thick cloud. This caused large increases in reflection above the baseline curve, particularly in the later, cloudier phase of the monsoon when bright monsoon weather systems passed over the AMF site frequently, but also on one occasion in late January when unusually thick cloud was present.

5. Radiative flux scatter plots

From the discussion in the previous section, several relationships begin to become apparent between radiative fluxes and the meteorology by simply comparing their variations over time. However, it is possible to look more closely at these relationships by plotting the radiation data against their controlling meteorological variables, and thereby gain more insight into the behavior of the fluxes that determine the radiative divergences. The longwave radiative fluxes are discussed first, followed by the shortwave.

5.1. Longwave scatter plots

In Section 4.1, it was argued that temperature and CWV have opposing influences on the DLR at the surface. In this section, these influences are examined further, with guidance from the simple formula developed by Prata (1996), which parametrizes the clear-sky DLR in terms of these two variables. Prata's formula is based on an analytic approximation to represent the dependence of the effective emissivity of the atmosphere on the CWV. In the paper, it was tested using both radiative transfer calculations and datasets of simultaneous measurements of air temperature, vapor pressure and DLR. The formula represents the average dependence across the globe of DLR on temperature and CWV, which provides a useful background with which the Niamey data may be compared. However, the very fact that the Niamey data include unusual combinations of

temperature and CWV means that one cannot expect the Prata formula to represent the flux data accurately, so care must be taken in the interpretation of the results shown below.

Prata's formula for the DLR at the surface may be written as;

$$\text{DLR} = \varepsilon \sigma T^4 \quad (1)$$

where σ is the Stefan-Boltzmann constant, T is the screen-level temperature and the effective emissivity of the atmosphere ε is approximated as;

$$\varepsilon \approx 1 - (1 + u) \cdot \exp\{-(1.2 + 3.0 u)^{0.5}\} \quad (2)$$

where u is the CWV in units of g cm^{-2} . The values of the DLR are thus calculated from two variables, the screen-level temperature T and the column water vapour u .

The symbols on the upper panels of Figures 5 and 6 show the values of the daily mean DLR measured at the Niamey airport site scatter-plotted against the observed screen-level T (Figure 5) and against the observed CWV (Figure 6). The symbols are colored according to whether the observations were made during the dry or wet seasons. In addition, the dotted lines show the values of DLR predicted by equations 1 and 2, where in each plot the dependence on either T or CWV is shown for several values of the other input variable. This provides a series of "Prata curves" that illustrate the expected dependence of the DLR on T and CWV for a range of input values that correspond to the conditions encountered in Niamey through the year. The lower panels in Figures 5 and 6 show simplified versions of the trajectories of the observed values of the DLR through the year, which summarise the seasonal variations of the observations and their dependence on T and CWV.

Figure 5 shows that the DLR increases with air temperature, as expected, but two complications are apparent. Firstly, the wet season fluxes are much higher than those during the dry season at the same air temperature, because the column water vapor (and hence the effective emissivity of the atmosphere) was much larger at this time of year. Secondly, the slope of the wet season fluxes is much lower than that during the dry season and the data points cross the Prata curves. This is because the lowest temperatures occurred in August, when the CWV was a maximum, whereas the highest temperatures in May were associated with somewhat lower CWV, as noted earlier. In addition, there was much more cloud late in the season, which further increased the emission to the surface at that time. Taken together, these factors lead to a much lower slope in the wet

season, as the data points move across the Prata lines for constant values of CWV.

The lower panel in Figure 5 illustrates the trajectory of the data points. At the beginning of the year, temperatures were around 25 °C and increased through the first dry season to around 35 °C whilst the DLR points moved onto a slightly lower Prata curve. With the monsoon onset, temperatures remained high but the DLR points jumped up to the 4 cm CWV Prata curve, after which the temperatures decreased. In late summer, the column water vapour was at its highest, but the temperature continued to fall, moving the DLR down the highest Prata curve. After the monsoon retreat, the temperature returned to around 30 °C, but the CWV fell, moving the DLR back to the lower Prata curves. As the year came to an end, the falling temperatures and CWV brought the DLR to its lowest values by moving it down more steeply than predicted by the Prata formula. Cloud had additional effects on the DLR, but did not change this basic result.

The dependence of the DLR on CWV is illustrated in Figure 6. The Prata equations predict that the effective emissivity of the atmosphere and hence the DLR should increase with CWV. This is broadly true for the data points, but again these cluster into separate groups for the two seasons. In this plot, the trajectory of the points is very different in the two dry seasons, as shown in the lower panel. During the first dry season from January to April, air temperatures increased by approximately 10 °C as the CWV decreased, moving the DLR onto progressively higher Prata curves but *backwards* on the CWV axis. With the monsoon onset, temperatures remained high, so the DLR followed the highest Prata curve in the direction of increased column water vapor, reaching about 4 cm in May. Thereafter, despite steadily increasing CWV, the DLR dropped as temperatures fell, moving the points onto a lower Prata curve in August. Following the monsoon retreat in October, the DLR dropped suddenly as both temperature and CWV fell, moving the data points to their lowest values and following a trajectory very different from that in the first dry season, but more in line with that predicted by the Prata formula.

Figures 5 and 6 provide valuable insights into how the opposing influences of changes in temperature and CWV led to the observed seasonal changes in the DLR. A similar analysis is now applied to the net longwave radiation at the surface and to the OLR, providing further background for the divergencies presented in Section 6 and for the analysis in Section 7, in which the effects on the radiative divergences are interpreted within the framework of a simple model of the greenhouse effect.

Figure 7 shows scatter plots of the net longwave radiation at the surface against temperature and CWV. The effect of the very different behavior of the DLR in the dry and wet seasons seen in Figure 5a is apparent in Figure 7a. In the dry seasons, the dependence of the DLR on temperature shown in Figure 5a roughly follows the Prata curves, with the result that the net radiation becomes only slightly more negative as the air temperature increases (Figure 7a). In contrast, the very different slope in the wet season seen in Figure 5a translates into a strong increase of the surface longwave cooling with temperature. The cooling is largest at the start of the wet season, when temperatures are highest but the CWV is still relatively low, and is lowest in August when temperatures have dropped but the atmosphere is at its most opaque (see also Figure 2c).

The difference between the dry and wet seasons is less apparent when the net longwave radiation is scattered against CWV (Figure 7b), as was also the case with the DLR. Here, the behavior is very much as expected, despite the scatter, with a steady reduction in the surface cooling as the CWV increases and the smallest values associated with cloudy days during the wet season.

The final component of the longwave radiation budget is the OLR, scatter plots for which are shown in Figure 8. The dependence on the screen-level air temperature is weak, with considerable scatter, particularly in the wet season when the atmosphere was more cloudy (Figure 8a), but there is some evidence of an increase in OLR with air temperature that is most apparent in the dry season. The isolated group of points with the highest values of OLR correspond to early April, just before the false monsoon onset, when the column water vapor was smallest and so the transmission of the surface emission to space was at a maximum.

Figure 8b also shows considerable scatter, but it does demonstrate that OLR decreases with increasing column water vapour, as would be expected. While it would be difficult to fit a reliable trend line through these data, it is important to note that the dependence of the OLR on CWV is roughly a mirror image of that for the surface net longwave shown in Figure 7b. This implies that the rate at which the atmosphere increases its net emission to the surface as CWV increases is roughly matched by the rate at which it traps the OLR. This compensation between the dependence of the surface net longwave and of the OLR on the CWV provides the key to understanding the behavior of the atmospheric longwave divergence, as is shown later.

In most locations, one would not expect to find a significant dependence of the longwave fluxes on aerosol loadings, either because the mass loadings are too low or because the aerosol is too

small to have an appreciable impact on thermal radiation. In the region of Niamey, however, the impact can be large (e.g. Slingo et al. 2006). To investigate this, Figure 9 shows scatter plots of the DLR at the surface and of the OLR against the aerosol extinction, defined as;

$$\text{extinction} = 1 - \exp(-\tau) \quad (3)$$

where τ is the aerosol optical thickness from the Banizoumbou AERONET site at 870nm. Extinction is used here because of the large range of values of optical thickness encountered through the year. Figure 9a shows that there is a measurable dependence of the DLR at the surface on aerosol, at least in the dry season when the effective emissivity of the atmosphere is low. In the wet season, the dependence is masked by the much larger changes in the other variables. The OLR is less sensitive, which is to be expected as the aerosol is mainly found in the lowest layers of the atmosphere. For comparison, the dotted lines show the fluxes computed by Turner (2008) for aerosol spheres consisting of Kaolinite (the most common mineral found in his retrievals), embedded in an atmospheric profile typical of the first dry season. The 11 micron optical thicknesses used by Turner were converted to the values of the extinction at 870nm shown in Figure 9 using an assumed Angstrom coefficient of 0.326, which Turner obtained when he compared his 11 micron retrievals with the Banizoumbou AERONET data at 1.02 microns. Figure 9 shows that the shapes of the simulated curves fit the data well, although the simulations are somewhat lower than the observed fluxes.

5.2. Shortwave scatter plots

The main factors that control the shortwave fluxes are more apparent in the timeseries than is the case for the longwave fluxes, as was shown in Section 4. For example, the modulation of the fluxes by the incoming solar radiation at the TOA and the signals of clouds and major aerosol events are very clear in Figures 3 and 4. One complication is the significant seasonal variation in the surface albedo, which was highest in the dry season and lowest in the wet season as the surface became wetter and vegetation grew (McFarlane et al. 2008, Settle et al. 2008). Another complication is scattering by aerosols and clouds, which makes it difficult to perform as simple an analysis for the individual fluxes as in the longwave. Nevertheless, a few scatter plots are used here to illustrate the effects of the CWV and aerosol loadings in the shortwave. In these plots, the daily fluxes are normalized by the value of the insolation at the TOA on that day. To first order, this removes the external astronomical control on the solar fluxes, leaving the meteorological

controls to show their influence more clearly in the scatter plots. The normalised downward shortwave radiative flux at the surface thus becomes the effective solar transmittance and the normalised reflected shortwave flux at the TOA becomes the albedo.

Figure 10a shows a scatter plot of the normalized downwelling shortwave flux at the surface (i.e. the transmittance) against the CWV. The distribution of points is highly skewed, with low values mainly due to cloud but also to aerosol events. However, the upper envelope of the points follows a clear trend downwards with increasing CWV. This trend is due to water vapor absorption, as may be seen by comparing the points with the solid line, which shows the broadband transmittance predicted by the modified Lacis-Hansen scheme developed by Ramaswamy and Freidenreich (1992, their Section 2 and Table 2). This line takes no account of scattering, either within the atmosphere or from the surface, but it does illustrate that the trend of the observations is consistent with increasing amounts of water vapor absorption.

The corresponding scatter plot against the aerosol extinction at 870nm, for clear skies only, is shown in Figure 10b. The data points again follow a downward trend and two curves are also plotted to assist the interpretation. The first shows the linear fit to the transmittance as a function of the aerosol optical thickness, obtained by McFarlane et al. (2008, their Figure 11), except that here the transmittance is forced to be unity at zero optical thickness (**we need to make a small Angstrom correction as they use 523nm**);

$$T_1 = 1 - 0.12 * \tau \quad (4)$$

The second curve is given by the analytical expression from the two-stream equations for the transmittance of a slab composed of conservative scatterers (i.e. the single scatter albedo is 1);

$$T_2 = 1 - (1-f) * \tau / \{1 + (1-f) * \tau\} \quad (5)$$

Where f is the fraction of the radiation that is forward scattered in a single event, given by $(1-f) = (1-g)/2$, where g is the asymmetry parameter. McFarlane et al. (2008) retrieved a mean value of 0.67 for g, giving $f=0.835$, which is used in Equation 5.

The two curves are in good agreement with each other and are consistent with the trend of the data, except that most of the data points lie below the two curves at low values of the extinction (low optical thickness), particularly during the wet season. This is probably due to the fact that

such clear conditions tend to be associated with higher values of the CWV (true?), which Figure 10a shows will tend to have lower transmittances as a result of absorption by water vapor.

Finally, Figure 11 shows similar plots for the albedo at the TOA (calculated by normalizing the reflected shortwave flux measured by GERB by the calculated incoming shortwave flux), as a function of CWV and aerosol extinction. Figure 11a shows a negative relationship between the albedo and the CWV, although at higher water vapor loadings the atmosphere is more frequently cloudy, which greatly increases the albedo. The magnitude of the trend is consistent with that in Figure 10a, suggesting the impact of water vapor absorption, but seasonal changes in the surface albedo may also be contributing, since the highest albedo occurs in the dry season and the lowest at the end of the wet season.

Figure 11b shows no clear dependence of the TOA albedo on the aerosol extinction at low optical thickness, but there is a marked trend towards higher albedos for optical thicknesses above about 0.5. The data point on the extreme right is for 8 March, during the major dust storm, when the albedo was enhanced considerably by the dust (Slingo et al. 2006). The other points on the right all correspond to significant dust events, which may also be seen by comparing Figure 1b with the reflected shortwave flux shown in Figure 4b. As with Figure 11a, there is a separation between the data points for the two seasons, which again points to an additional influence from changes in the surface albedo. Some data points that are well above the general trend are associated with days when the cloud mask failed to identify significant amounts of cloud that had a large impact on the GERB shortwave fluxes.

6. Radiative divergences

Having analyzed the component fluxes and discussed the factors that control them, this section presents the longwave, shortwave and net radiative divergences, obtained by combining the ARM surface data with the GERB data from space. This realises one of the major goals of the RADAGAST project. Divergence is defined as the net radiation into a level, so that positive values imply heating and negative values imply cooling. Surface divergence is therefore defined as the downwelling minus the upwelling radiation, corresponding to the net radiation into the surface. The TOA divergence is defined as the incoming minus outgoing radiation, i.e. the net radiation into the system. The atmospheric divergencies are obtained by subtracting those at the

surface from those at the TOA. The sign convention means that the longwave divergencies are all negative, corresponding to cooling, while the shortwave divergences are all positive, corresponding to heating. The net divergences are obtained by adding the shortwave and longwave components. Although some of the surface and TOA divergences have already been discussed in earlier sections (e.g. the OLR), plots are also shown here, not only for completeness but also to illustrate how their behavior determines that of the atmospheric divergences.

6.1. Timeseries of divergences

Figure 12 shows the daily mean longwave radiative divergences through the year. As was found earlier, the seasonal variations in the TOA and surface divergences follow a very similar pattern, with maximum cooling both from the surface and out to space at the end of the first dry season, when temperatures were highest and the CWV (and hence the atmospheric emissivity) at a minimum. In contrast, the high values of CWV in August lead to the smallest values of the surface cooling and also the lowest values of the OLR. The effects at the TOA are strengthened by the cloudiness maximum at this time of year, although clouds also had a significant impact in the dry seasons.

The most remarkable feature in Figure 12 is the atmospheric divergence, which shows a much smaller variation through the year than the divergences at the TOA and at the surface. The small magnitude of this variation shows that most of the change in cooling at the TOA was made up of changes taking place at the surface, rather than in the atmosphere. From previous work (e.g. Stephens et al. 1994), one would expect the longwave cooling of the atmosphere to increase with the CWV, which does vary over a very large range in Niamey. However, while Figure 12 shows slightly higher cooling during the wet season than in the dry season, the magnitude of the difference is small. The reasons for this behavior are explored below.

Figure 13 shows the corresponding divergences in the shortwave. The upper envelope of these curves is clearly controlled by the seasonal variation in the daily mean insolation at the TOA (compare with Figure 4c). As in the longwave, the shortwave divergences at the TOA and at the surface follow each other through the year, while the atmospheric divergence shows a smaller variation, although in the second dry season all three divergences show the same decline. Clouds produce the largest short term signals, but the magnitudes at the TOA and at the surface are similar, so that the effect of clouds tends to cancel in the atmospheric absorption, consistent with

the expectation that clouds do not make a major contribution to atmospheric absorption in the shortwave (ref). In contrast, comparison of Figure 13 with Figure 1b shows that aerosol events impact the surface divergence more than at the TOA, so that peaks in the atmospheric heating coincide closely with peaks in aerosol optical thickness. The drop in the atmospheric divergence in the second dry season could be related to the observed reduction in aerosol, but it must also be remembered that the CWV is low at this time of year, which would also reduce the absorption.

6.2. Scatter plots

It was shown in Section 5 that the effects of temperature and CWV have opposing influences on the DLR and net longwave radiation at the surface, and also on the OLR. The dependence on temperature was quite complicated, with different behaviors in the dry and wet seasons. The dependence on CWV was broadly as would be expected: a reduction in both the surface and TOA cooling with increasing CWV. Consistent with these results, Figure 14 appears to show no discernible dependence of the atmospheric longwave divergence on temperature, but a weak dependence on the CWV. Unfortunately, given the strong negative correlation between temperature and CWV, it is very difficult to interpret these scatter plots further, because they do not allow the two effects to be separated. A methodology that allows such a separation and which explains the behavior shown in Figure 12 is introduced in Section 7.

While scatter plots cannot unravel the dependence of the longwave divergence on temperature and CWV, they are valuable for other variables. The dependence of the atmospheric longwave divergence on the aerosol extinction is shown in Figure 15. This shows a discernible trend towards greater longwave cooling as the aerosol loading increases, consistent with the results in Figure 9, which show that the downward longwave at the surface is more sensitive to aerosol than the OLR. This dependence is somewhat stronger in the dry seasons.

The atmospheric divergence in the shortwave clearly increases with CWV, particularly at the lowest humidities (Figure 16a). The shortwave absorption also increases with the aerosol loading (Figure 16b). This is mainly due to the reduced transmission to the surface (Figure 10b), because the TOA albedo actually shows an increase with the aerosol loading (Figure 11b), a characteristic feature of weakly absorbing aerosols.

Figure 17 shows that over the course of the year, the region neither gains nor loses much radiative energy at the TOA. The net radiation varies between the seasons, with the region

gaining energy during boreal summer and experiencing a net energy loss during boreal winter. However, the surface gains radiative energy at all times of the year, but particularly during the summer monsoon, whilst the atmosphere continually loses heat to space and to the surface at a steady rate of around 80 Wm^{-2} , increasing in the second dry season.

It would be good to mention the surface fluxes, cross referencing to Miller et al. (2008), and the balance from atmospheric advection to complete the picture. This could be summarised in a table, and/or in an additional, schematic figure, but it should not duplicate Miller et al. (2008).

7. Interpretation of the longwave fluxes and divergences using a simple model

One of the most remarkable results from this study is the compensation between the effects of changes in temperature and column water vapor on the longwave fluxes and atmospheric divergences. These changes are negatively correlated for much of the year, so the scatter plots do not allow the effects to be separated unequivocally from each other. In this section, we examine this result further and provide such a separation with the help of a simple model of the greenhouse effect. This employs a version of the methodology of Stephens et al. (1994).

Let the longwave atmospheric flux divergence be denoted by ΔF . Stephens et al. (1994) write this in terms of the component fluxes as;

$$\Delta F = \sigma T_s^4 - F_\infty - F_g \quad (6)$$

where the first term is the upward longwave flux from the surface, the second term is the outgoing longwave radiation (OLR) and the third term is the DLR at the surface.

The problem with (6) in this form is that the second and third terms depend both on temperature and on the atmospheric emissivity (which for clear-skies is largely controlled by the column water vapor, CWV). To deal with this, Stephens et al. (1994) introduced two dimensionless parameters that normalise these two fluxes. Their choice of normalisation was motivated by the desire to use observed quantities (in their case σT_s^4 and OLR) to estimate the surface fluxes and atmospheric divergence from readily available global sea surface temperature and OLR datasets. Here, since the main purpose is to separate the effects of temperature and column water vapor, we choose different normalisations that simplify the subsequent interpretation.

The first dimensionless parameter is the normalised greenhouse effect, G , defined here as;

$$G = F_{\infty} / \sigma T_s^4 \quad (7)$$

This is smaller than unity in most cases, reflecting the fact that the greenhouse effect acts to reduce the emission to space, compared with that from the surface.

Similarly, the second dimensionless parameter is defined as;

$$F = F_g / \sigma T_s^4 \quad (8)$$

This is also smaller than unity, because the downward longwave radiation from the atmosphere is generally smaller than the emission from the surface. Comparison with Equation 1 shows that F is equivalent to ε in the Prata formula.

Substituting 7 and 8 into 6 leads to;

$$\Delta F = \sigma T_s^4 (1 - G - F) \quad (9)$$

where the value of ΔF is generally negative, because on average the net effect of longwave radiation is to cool the atmosphere.

To first order, Equation 9 separates the effects of temperature (the first term) from those of atmospheric emissivity (the term in parentheses), although this is only approximate as in reality both F_{∞} and F_g depend on the full vertical profiles of both temperature and humidity.

The study by Stephens et al. (1994) concentrated on clear-sky data over the oceans. They showed that the magnitudes of the greenhouse effect and of the clear-sky atmospheric longwave cooling increased with both sea surface temperature and column water vapor. This behavior is largely controlled by the Clausius-Clapeyron equation: over the oceans, the column water vapor (and hence the effective emissivity of the atmosphere) is lowest at cold, high latitudes and highest at warm, low latitudes. As a result, column water vapor and temperature are positively correlated when global data are considered, as shown by Stephens (1990). In contrast, over Niamey the column water vapor is controlled much less by the air temperature than by the atmospheric dynamics, so that the lowest values occur when the hot, dry Harmattan wind blows from the deserts, while the highest values occur during the wet season, when the air blows from the Gulf of Guinea. The net effect is that temperature and column water vapor are negatively correlated for most of the year, leading to the unusual impact on the longwave fluxes and heating rates found in this study.

To illustrate the impact on the longwave atmospheric divergence, scatter plots of G , F and $1-G-F$ against CWV are shown in Figure 18. Although there is some scatter, this figure demonstrates that the dependence on the CWV of the normalized greenhouse effect and of the atmospheric emissivity seen from the surface are virtually mirror images of each other, so that the $1-G-F$ term in Equation 9 is almost independent of CWV. As the CWV increases, the atmosphere thus loses longwave radiation to the surface with the same increasing efficiency with which it traps the outgoing OLR. The timeseries of these terms shown in Figure 19 illustrates the compensation between G and F through the year and the approximate constancy of $1-G-F$. The remarkably small variation in the atmospheric longwave divergence through the year is thus due to the approximate cancellation between the normalized greenhouse effect G and the atmospheric emissivity seen from the surface F , which removes most of the dependence of the atmospheric cooling on the CWV, so that the remaining variations through the year of the divergence come from the relatively smaller changes in the σT_s^4 and $1-G-F$ terms in Equation 9.

One complication: regarding the compensation between the dependence of the DLR and OLR on CWV shown in Figures 7b and 8b, the OLR decrease must be due to increases in mid and upper tropospheric humidity, which can perhaps be seen in Figure 8 of Part 1 and should be mentioned. This is another example of something that could be investigated using some controlled numerical experiments with radiation codes (to be mentioned under future work).

8. Discussion and conclusions

To be completed.

Further work:

One thing to suggest is to see whether the longwave compensation between temperature and CWV happens in other datasets. One would be the ERA40 reanalysis, or even better the new ERA-Interim reanalysis, and the other would be the HiGEM model (which of course has aerosols included, so that aspect could be looked at, whereas it can't in the reanalyses, yet). Questions that these investigations could address include: is the compensation a one-off that happened only in 2006, or does it happen every year in the reanalyses? Can a climate model reproduce the

relationships found here? Can we perform a similar analysis at other ARM sites, using estimates of the broadband fluxes from narrow band geostationary data? It would be good to refer to McFarlane et al. (2007) in making that point and also to say that it would also be good to have vertical heating rates.

Acknowledgments. We thank Didier Tanré for his efforts in establishing and maintaining the Banizoumbou AERONET site. The AMF data were obtained by the Atmospheric Radiation Measurement (ARM) Program, which is funded by the Office of Biological and Environmental Research, Office of Science, U.S. Department of Energy. Edition 1 GERB data were obtained from the GERB Ground Segment Processing System (GGSPS) at the Rutherford Appleton Laboratory, UK. We also thank XXX for comments on the manuscript. Anthony Slingo is supported by the National Centre for Earth Observation of the UK Natural Environment Research Council (NERC) and Gary Robinson is also supported by NERC. Helen White is funded by a NERC studentship and Nazim Ali Bharmal by NERC grant number NE/D002370/1.

References

- Bell, M. A. and P. J. Lamb, 2006. Integration of weather system variability to multidecadal regional climate change: the West African Sudan-Sahel zone, 1951-98. *J. Climate*, **19**, 5343-5365
- Bharmal, N. A., A. Slingo, G. J. Robinson and J. J. Settle, 2008. Simulation of surface and top of atmosphere thermal fluxes and radiances from the RADAGAST experiment. *J. Geophys. Res.*, to be submitted for publication
- Charney, J. G., 1975. Dynamics of deserts and drought in the Sahel. *Q. J. R. Meteorol. Soc.*, **101**, 193-202
- Comer, R. E., A. Slingo and R. P. Allan, 2007. Observations of the diurnal cycle of outgoing longwave radiation from the Geostationary Earth Radiation Budget instrument. *Geophys. Res. Lett.*, **34**, L02823, doi:10.1029/2006GL028229
- Derrien, M., and H. Le Gléau, 2005. MSG/SEVIRI cloud mask and type from SAFNWC. *Int. J. Remote Sens.*, **26**, 4707-4732, DOI: 10.1080/01431160500166128
- Dewitte, S., L. Gonzalez, N. Clerbaux, A. Ipe, C. Bertrand and B. De Paepe, 2008. The Geostationary Earth Radiation Budget Edition 1 data processing algorithms. *Advances in Space Research*, **41**, No. 11, 1906-1913
- Harries, J. E. and 42 authors, 2005. The Geostationary Earth Radiation Budget (GERB) project. *Bull. Am. Meteorol. Soc.*, **86**, 945-960
- Haywood, J. M, et al., 2008. Overview of the Dust and Biomass burning Experiment and African Monsoon Multidisciplinary Analysis Special Observing Period-0. *J. Geophys. Res.*, submitted for publication in DABEX special section
- Holben, B. N., et al., 2001. An emerging ground-based aerosol climatology: Aerosol Optical Depth from AERONET, *J. Geophys. Res.*, **106**, 12067-12097
- Kiehl, J. T. and Trenberth, K. E., 1997. Earth's annual global mean energy budget. *Bull. Amer. Meteorol. Soc.*, **78**, 197-208
- Kollias, P., M. Miller and K. L. Johnson, 2008. Cloud and precipitation observations during the 2006 ARM Mobile Facility deployment in Niamey, Niger, Africa. *J. Geophys. Res.*, to be submitted for publication

- Loeb, N. G., B. A. Wielicki, W. Su, K. Loukachine, W. Sun, T. Wong, K. J. Priestley, G. Matthews, W. F. Miller and R. Davies, 2007. Multi-instrument comparison of top-of-atmosphere reflected solar radiation. *J. Clim.*, **20**, 575-591
- McFarlane, S. A., J. H. Mather and T. P. Ackerman, 2007. Analysis of tropical radiative heating profiles: A comparison of models and observations. *J. Geophys. Res.*, **112**, D14218, doi:10.1029/2006JD008290
- McFarlane, S. A., E. I. Kassianov, J. Barnard, C. Flynn and T. P. Ackerman, 2008. Surface shortwave aerosol radiative forcing during the ARM Mobile Facility deployment in Niamey, Niger. *J. Geophys. Res.*, to be submitted for publication
- Miller, M. A. and A. Slingo, 2007. The ARM Mobile Facility and its first international deployment: measuring radiative flux divergence in West Africa. *Bull. Am. Meteorol. Soc.*, **88**, 1229-1244
- Miller, R. L., J. Barnard, E. Kassianov and A. Slingo, 2008. Seasonal contrasts in the surface energy balance of the Sahel. *J. Geophys. Res.*, to be submitted for publication
- Ohmura, A., et al., 1998. Baseline Surface Radiation Network (BSRN/WCRP): New precision radiometry for climate research. *Bull. Am. Meteorol. Soc.*, **79**, 2115-2136
- Prata, A. J., 1996. A new long-wave formula for estimating downward clear-sky radiation at the surface. *Q. J. R. Meteorol. Soc.*, **122**, 1127-1151
- Prospero, J. M., P. Ginoux, O. Torres, S. E. Nicholson and T. E. Gill, 2002. Environmental characterization of global sources of atmospheric soil dust identified with the Nimbus 7 total ozone mapping spectrometer (TOMS) absorbing aerosol product. *Rev. Geophys.*, **40**, 1002, doi:10.1029/2000RG000095
- Ramana, M. V., V. Ramanathan, D. Kim, G. C. Roberts and C. E. Corrigan, 2007. Albedo, atmospheric solar absorption and heating rate measurements with stacked UAVs. *Q. J. R. Meteorol. Soc.*, **133**, 1913-1931
- Ramaswamy, V. and S. M. Freidenreich, 1992. A study of broadband parameterizations of the solar radiative interactions with water vapor and water drops. *J. Geophys. Res.*, **97**, D11, 11487-11512
- Randall, D. A., et al., 2007. Climate Models and Their Evaluation. In: *Climate Change 2007: The Physical Science Basis. Contribution of Working Group I to the Fourth Assessment Report*

of the Intergovernmental Panel on Climate Change [Solomon, S., D. Qin, M. Manning, Z. Chen, M. Marquis, K. B. Averyt, M. Tignor and H. L. Miller (eds.)]. Cambridge University Press, Cambridge, United Kingdom and New York, NY, USA

Redelsperger, J.-L., C. D. Thorncroft, A. Diedhiou, T. Lebel, D. J. Parker and J. Polcher, 2006. African Monsoon Multidisciplinary Analysis. An international research project and field campaign. *Bull. Am. Meteorol. Soc.*, **87**, 1739-1746

Schmetz, J., P. Pili, S. Tjemkes, D. Just, J. Kerkman, S. Rota, and A. Ratier, 2002. An introduction to Meteosat Second Generation (MSG). *Bull. Am. Meteorol. Soc.*, **83**, 977-992

Settle, J. J., N. A. Bharmal, G. J. Robinson and A. Slingo, 2008. Bounding the uncertainty of flux divergence calculations in RADAGAST. *J. Geophys. Res.*, to be submitted for publication

Slingo, A., et al., 2006. Observations of the impact of a major Saharan dust storm on the atmospheric radiation balance. *Geophys. Res. Lett.*, **33** (24), L24817, doi: 10.1029/2006GL027869

Slingo, A., et al., 2008. Overview of observations from the RADAGAST experiment in Niamey, Niger. Part 1: Meteorology and thermodynamic variables. *J. Geophys. Res.*, submitted for publication

Stackhouse, P. W., S. K. Gupta, S. J. Cox, J. C. Mikowitz, T. Zhang and M. Chiacchio, 2004. 12-year surface radiation budget data set. *GEWEX News*, **14**, 10-12

Stephens, G. L., 1990. On the relationship between water vapor over the oceans and sea surface temperature. *J. Clim.*, **3**, 634-645

Stephens, G. L., A. Slingo, M. J. Webb, P. J. Minnett, P. H. Daum, L. Kleinman, I. Wittmeyer and D. A. Randall, 1994. Observations of the Earth's radiation budget in relation to atmospheric hydrology. 4. Atmospheric column radiative cooling over the world's oceans. *J. Geophys. Res.*, **99**, 18585-18604

Turner, D. D., 2008. Ground-based infrared retrievals of optical depth, effective radius, and composition of airborne mineral dust above the Sahel. *J. Geophys. Res.*, submitted for publication

Wong, T., B. A. Wielicki, R. B. Lee, G. L. Smith, K. A. Bush, and J. K. Willis, 2006. Reexamination of the observed decadal variability of the earth radiation budget using altitude-corrected ERBE/ERBS nonscanner WFOV data. *J. Clim.* **19**, 4028-4040

Zhang, Y., W. B. Rossow, A. A. Lacis, V. Oinas and M. I. Mishchenko, 2004. Calculation of radiative fluxes from the surface to top of atmosphere based in ISCCP and other global data sets: Refinements of the radiative transfer model and the input data. *J. Geophys. Res.*, 109, D19105, doi:10.1029/2003JD004457

Figure captions

Should we include “daily mean” in each and every figure?

Figure 1. a) timeseries of cloud fraction derived from SEVIRI data for the GERB ARG pixel over Niamey (solid) and from the Kollias et al. (2008) cloud data (dashed). Note that the latter data are only available from mid-April. b) timeseries of aerosol optical thickness at 870nm from the AERONET site at Banizoumbou. The day number in 2006 is shown along the bottom of each plot. The dashed vertical lines denote the boundaries between the calendar months, the first letters of which are shown along the top of each plot.

Figure 2. Timeseries of the surface a) downwelling, b) upwelling and c) net longwave fluxes, measured at the AMF Niamey airport site. The day number in 2006 is shown along the bottom of each plot. The dashed vertical lines denote the boundaries between the calendar months, the first letters of which are shown along the top of each plot.

Figure 3. Timeseries of the surface a) downwelling, b) upwelling and c) net shortwave fluxes, measured at the AMF Niamey airport site. The day number in 2006 is shown along the bottom of each plot. The dashed vertical lines denote the boundaries between the calendar months, the first letters of which are shown along the top of each plot.

Figure 4. Timeseries of the top of atmosphere a) outgoing longwave radiation (OLR) measured by GERB, b) reflected shortwave radiation measured by GERB and c) calculated incoming shortwave radiation. The day number in 2006 is shown along the bottom of each plot. The dashed vertical lines denote the boundaries between the calendar months, the first letters of which are shown along the top of each plot.

Figure 5. a) scatter plot of the downwelling longwave flux at the surface, measured at the AMF Niamey airport site, against surface air temperature. The data points are color coded according to whether they were measured during the dry or wet seasons. Open squares denote days with cloud, according to the SEVIRI cloud mask. The dotted lines show the fluxes given by the Prata formula (Equations 1 and 2) for several values of the column water vapor (cm). b) simplified representation of the trajectory of the measurements through the year (see text).

Figure 6. a) scatter plot of the downwelling longwave flux at the surface, measured at the AMF Niamey airport site, against column water vapor. The data points are color coded according to whether they were measured during the dry or wet seasons. Open squares denote days with cloud,

according to the SEVIRI cloud mask. The dotted lines show the fluxes given by the Prata formula (Equations 1 and 2) for several values of the surface air temperature (K). b) simplified representation of the trajectory of the measurements through the year (see text).

Figure 7. Scatter plots of the net longwave flux at the surface, measured at the AMF Niamey airport site, against a) surface air temperature and b) column water vapor. In each panel, the data points are color coded according to whether they were measured during the dry or wet seasons. Open squares denote days with cloud, according to the SEVIRI cloud mask.

Figure 8. Scatter plots of the outgoing longwave radiation (OLR), measured by GERB, against a) surface air temperature and b) column water vapor. In each panel, the data points are color coded according to whether they were measured during the dry or wet seasons. Open squares denote days with cloud, according to the SEVIRI cloud mask.

Figure 9. Scatter plots of a) the downwelling longwave flux at the surface, measured at the AMF Niamey airport site and of b) the outgoing longwave radiation (OLR), measured by GERB, against the aerosol extinction at 870nm (defined by Equation 3). In each panel, the data points are color coded according to whether they were measured during the dry or wet seasons. Points are only plotted for days without cloud, according to the SEVIRI cloud mask. The dotted lines show the fluxes simulated by Turner (2008) for Kaolinite spheres (see text for details).

Figure 10. Scatter plots of the ratio of the downwelling shortwave flux at the surface, measured at the AMF Niamey airport site, to the insolation at the TOA, against a) the CWV and b) the aerosol extinction at 870nm (defined by Equation 3). In each panel, the data points are color coded according to whether they were measured during the dry or wet seasons. In a), open squares denote days with cloud, according to the SEVIRI cloud mask, and the dotted line shows the dependence of the water vapor transmittance on CWV, given by a simple parametrization (see text for details). For clarity, this line has been offset in the vertical so that it lies just above the data points. In b), points are only plotted for days without cloud, according to the SEVIRI cloud mask, and the solid line shows the transmittance given by Equation 4 and the dashed line shows that given by Equation 5. For clarity, both lines have been offset in the vertical.

Figure 11. Scatter plots of the ratio of the reflected shortwave flux at the TOA, measured by GERB, to the insolation at the TOA, against a) the CWV and b) the aerosol extinction at 870nm (defined by Equation 3). In each panel, the data points are color coded according to whether they were measured during the dry or wet seasons. In a), open squares denote days with cloud,

according to the SEVIRI cloud mask. In b), points are only plotted for days without cloud, according to the SEVIRI cloud mask.

Figure 12. Timeseries of the longwave radiative divergences, calculated from the component fluxes, for the Earth-atmosphere system as a whole (dotted), for the surface (dashed) and for the atmosphere (solid). The day number in 2006 is shown along the bottom of each plot. The dashed vertical lines denote the boundaries between the calendar months, the first letters of which are shown along the top of each plot.

Figure 13. Timeseries of the shortwave radiative divergences, calculated from the component fluxes, for the Earth-atmosphere system as a whole (dotted), for the surface (dashed) and for the atmosphere (solid). The day number in 2006 is shown along the bottom of each plot. The dashed vertical lines denote the boundaries between the calendar months, the first letters of which are shown along the top of each plot.

Figure 14. Scatter plots of the longwave radiative divergence across the atmosphere against a) air temperature and b) column water vapor. In each panel, the data points are color coded according to whether they were measured during the dry or wet seasons. Open squares denote days with cloud, according to the SEVIRI cloud mask.

Figure 15. Scatter plot of the longwave radiative divergence across the atmosphere against the aerosol extinction at 870nm (defined by Equation 3). The data points are color coded according to whether they were measured during the dry or wet seasons. Points are only plotted for days without cloud, according to the SEVIRI cloud mask.

Figure 16. Scatter plots of the shortwave radiative divergence across the atmosphere against a) column water vapor and b) aerosol extinction. In each panel, the data points are color coded according to whether they were measured during the dry or wet seasons. In a), open squares denote days with cloud, according to the SEVIRI cloud mask. In b), points are only plotted for days without cloud, according to the SEVIRI cloud mask.

Figure 17. Timeseries of the net radiative divergences, obtained by adding the longwave and shortwave components, for the Earth-atmosphere system as a whole (dotted), for the surface (dashed) and for the atmosphere (solid). The day number in 2006 is shown along the bottom of each plot. The dashed vertical lines denote the boundaries between the calendar months, the first letters of which are shown along the top of each plot.

Figure 18. Scatter plots of the dimensionless parameters G , F and $1-G-F$ (see text for definition) against the column water vapor CWV. In each panel, the data points are color coded according to whether they were measured during the dry or wet seasons. Open squares denote days with cloud, according to the SEVIRI cloud mask.

Figure 19. Timeseries of the dimensionless parameters G , F and $1-G-F$ (see text for definition). The day number in 2006 is shown along the bottom of each plot. The dashed vertical lines denote the boundaries between the calendar months, the first letters of which are shown along the top of each plot.

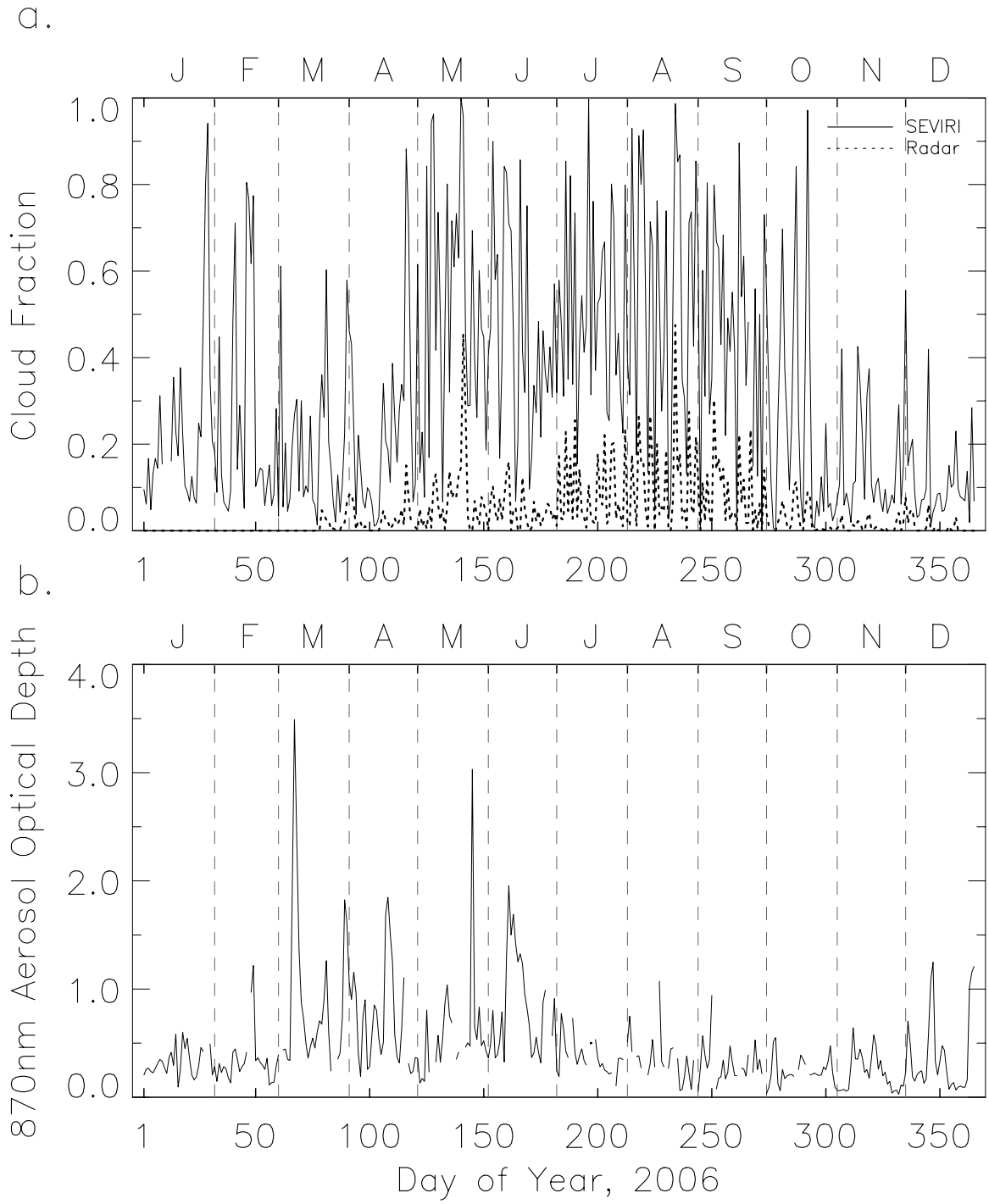


Figure 1

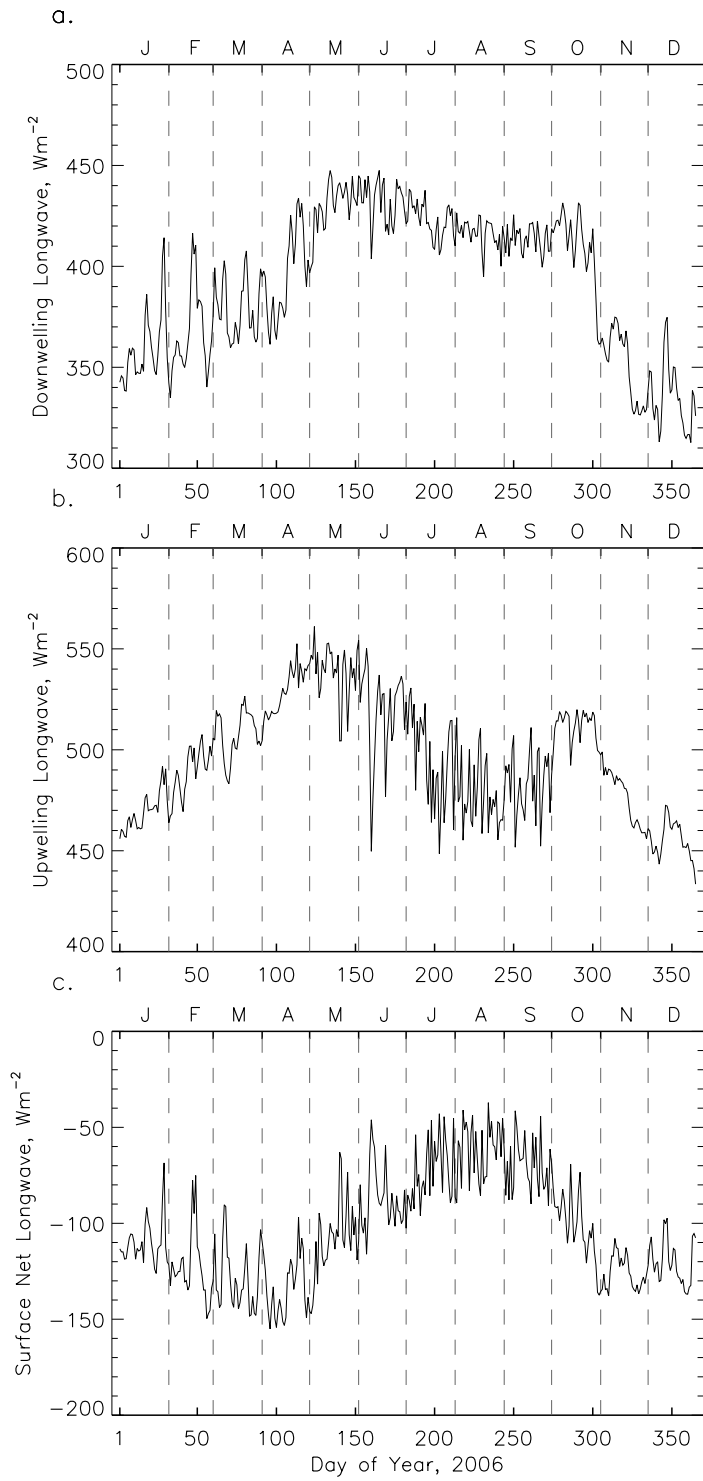


Figure 2

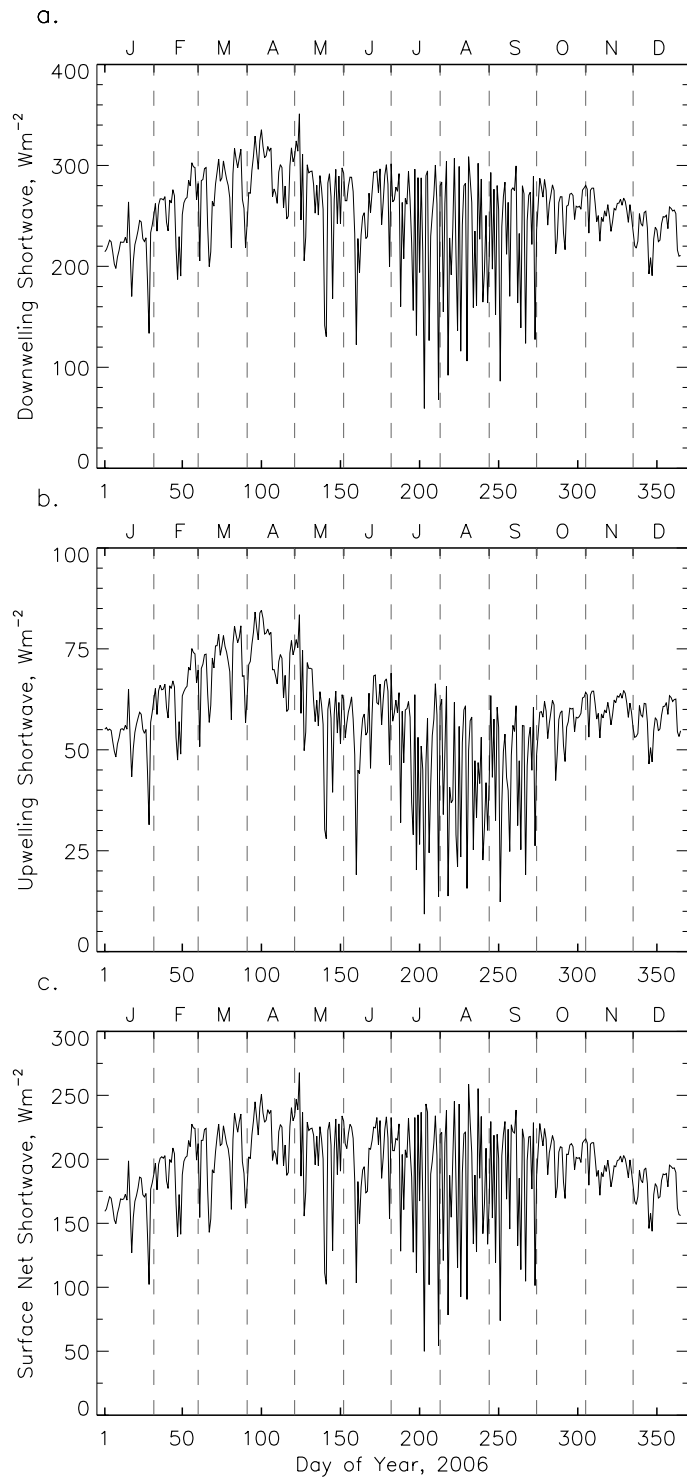


Figure 3

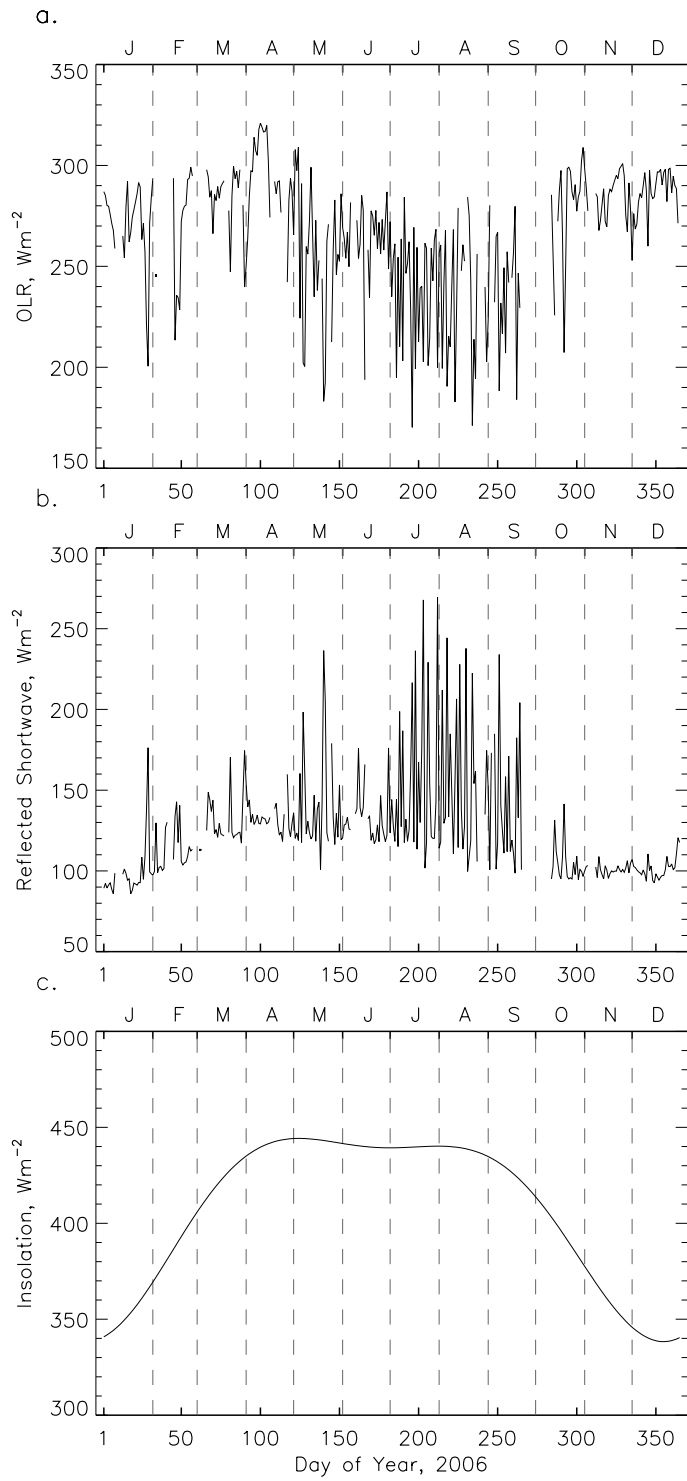


Figure 4

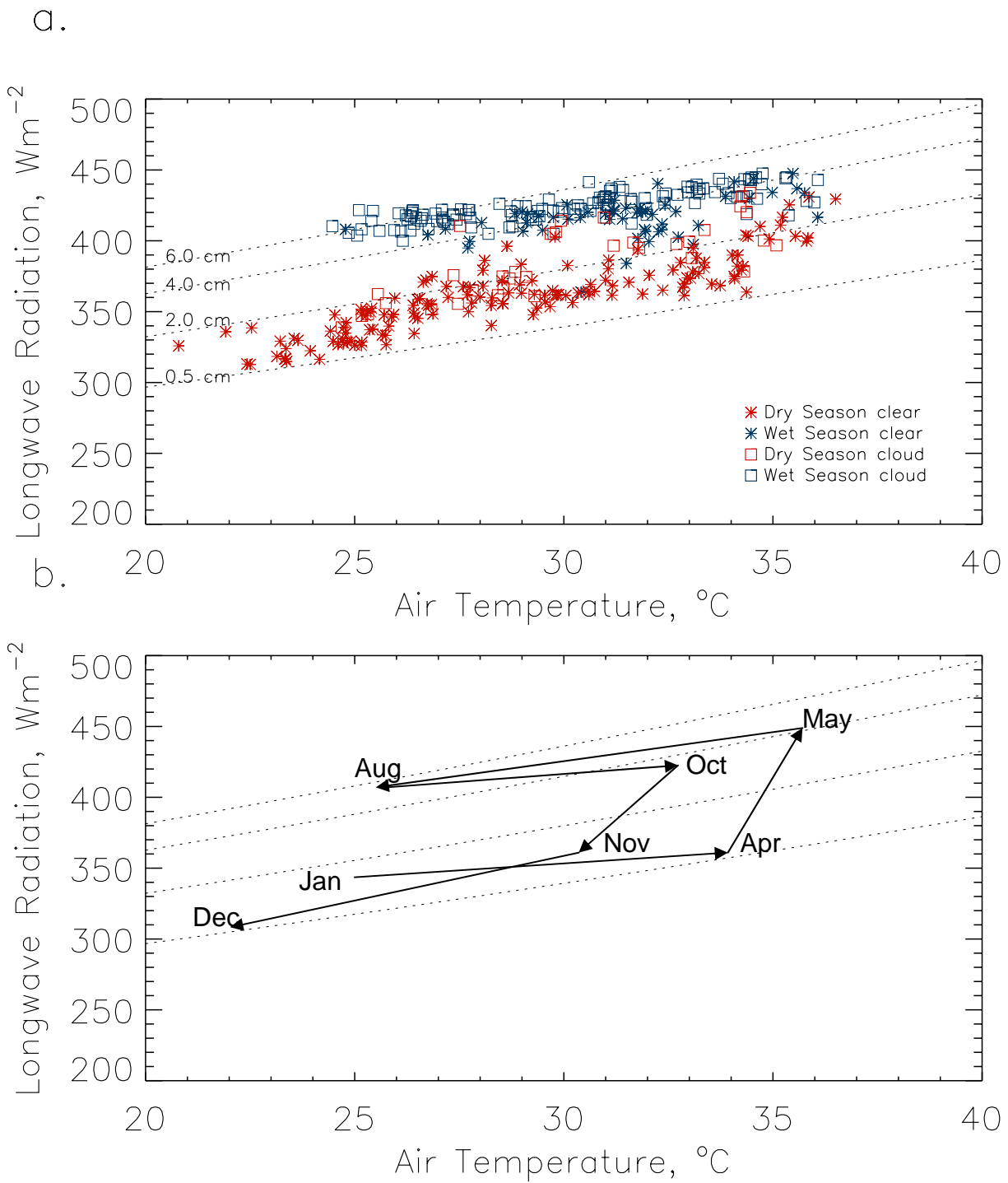


Figure 5

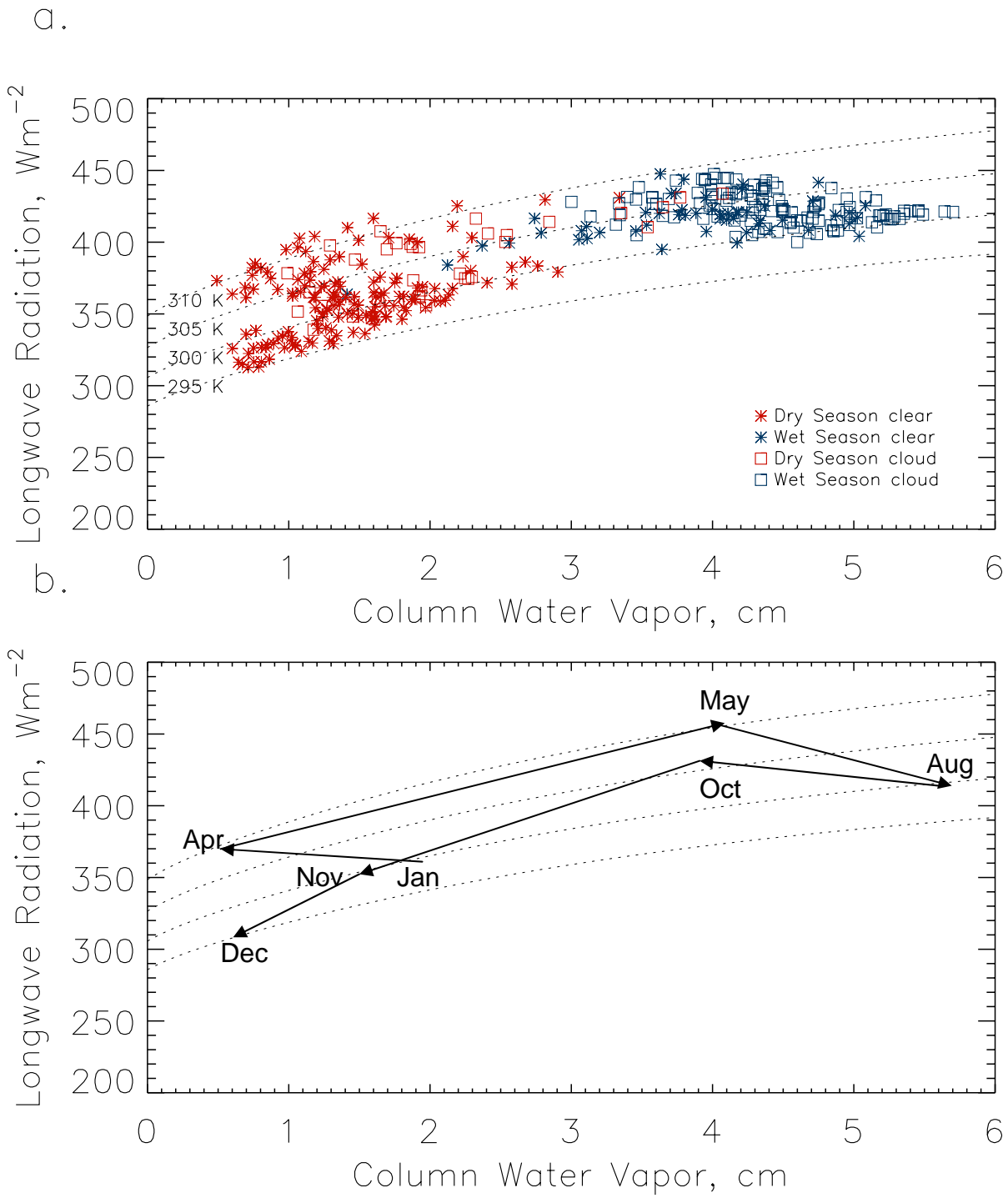


Figure 6

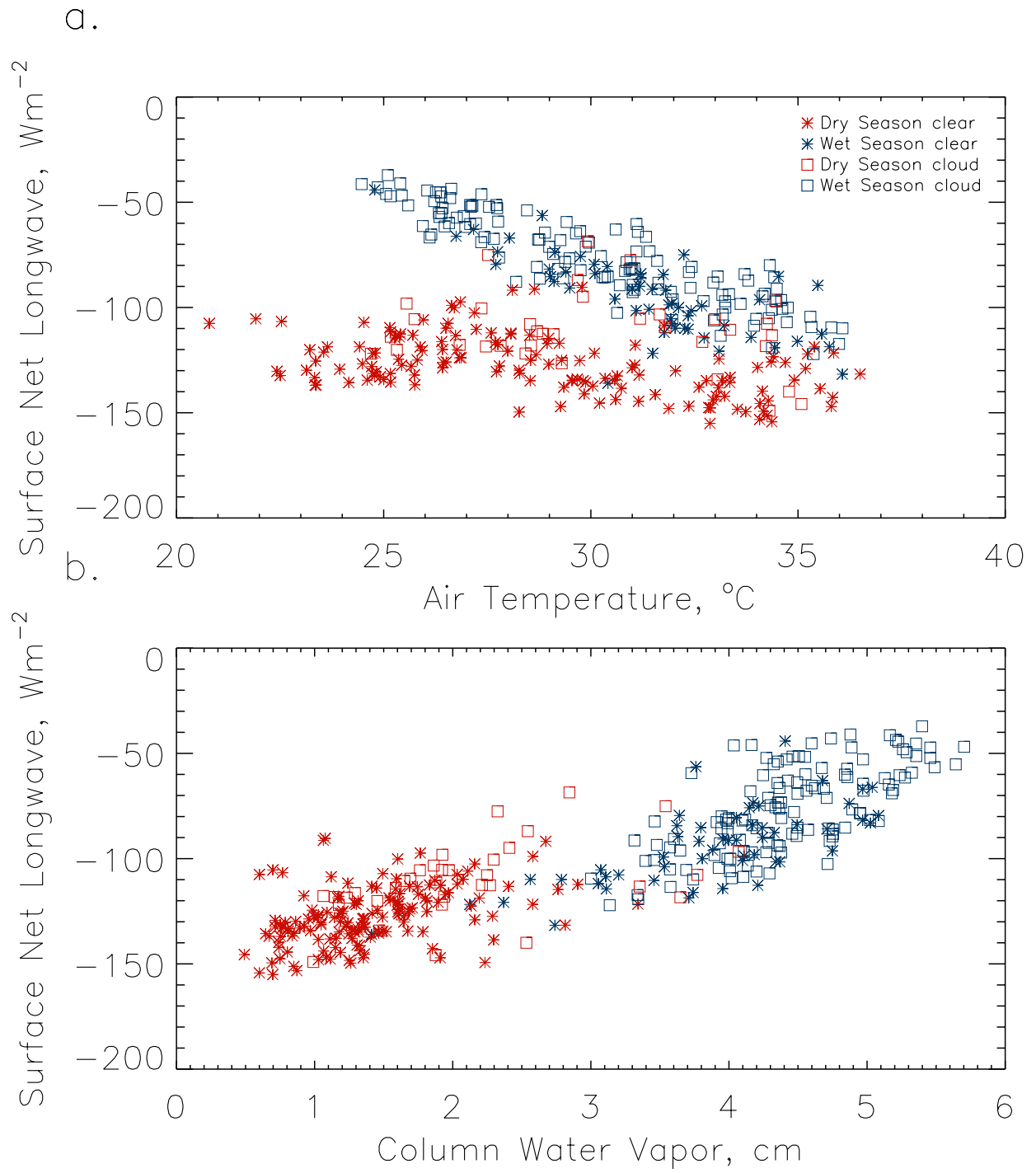


Figure 7

a.

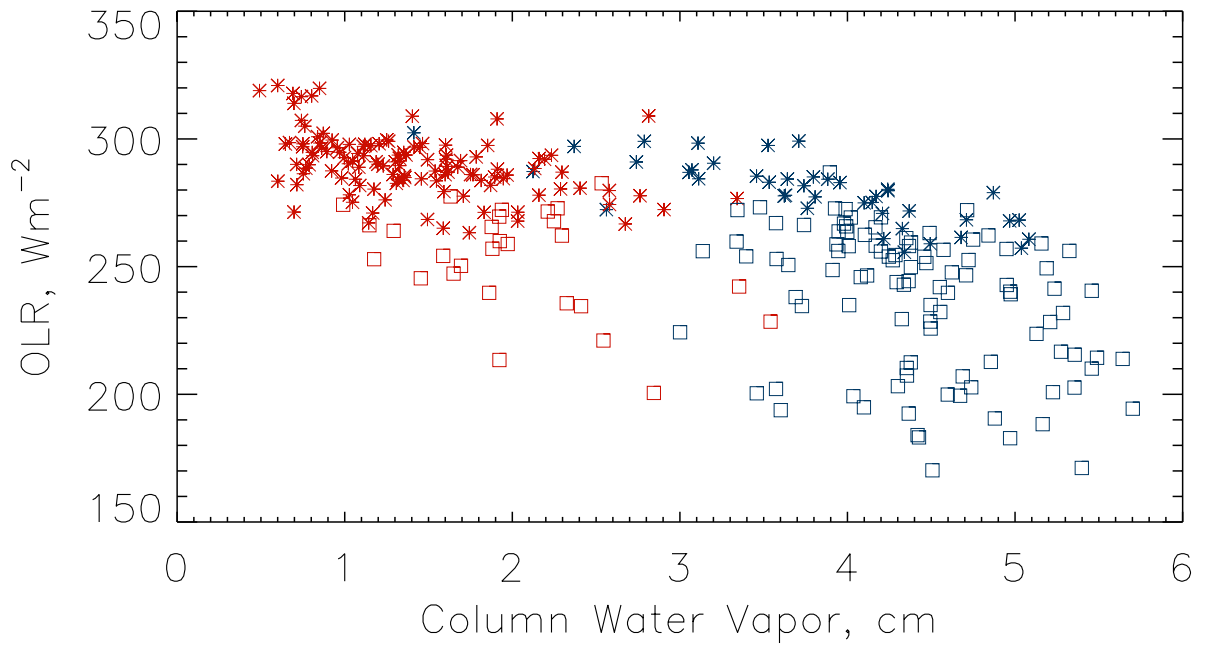
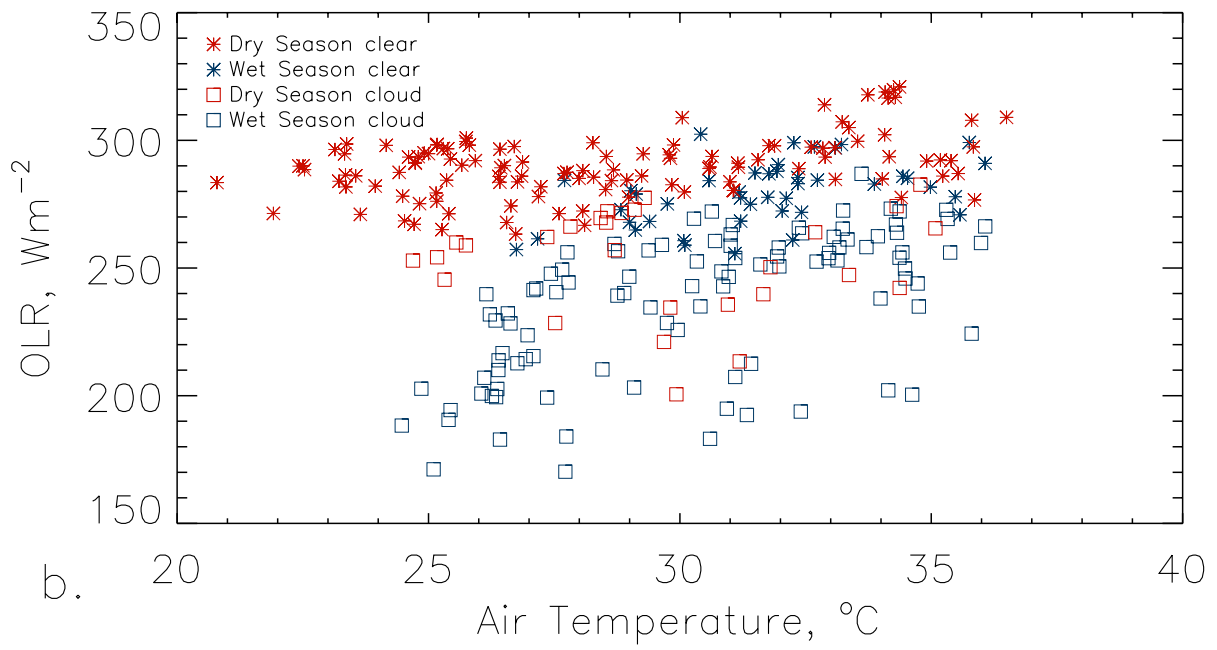


Figure 8

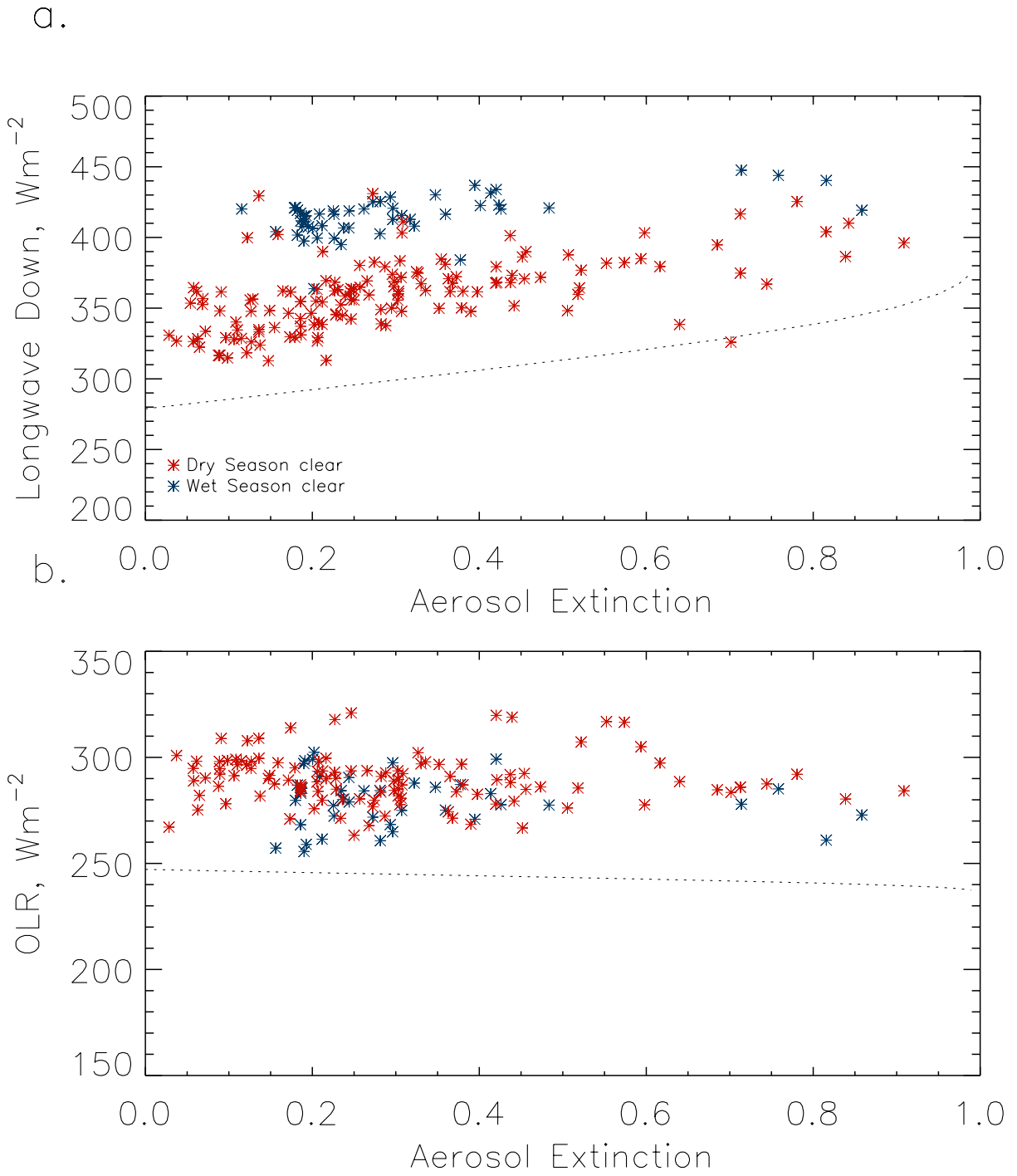
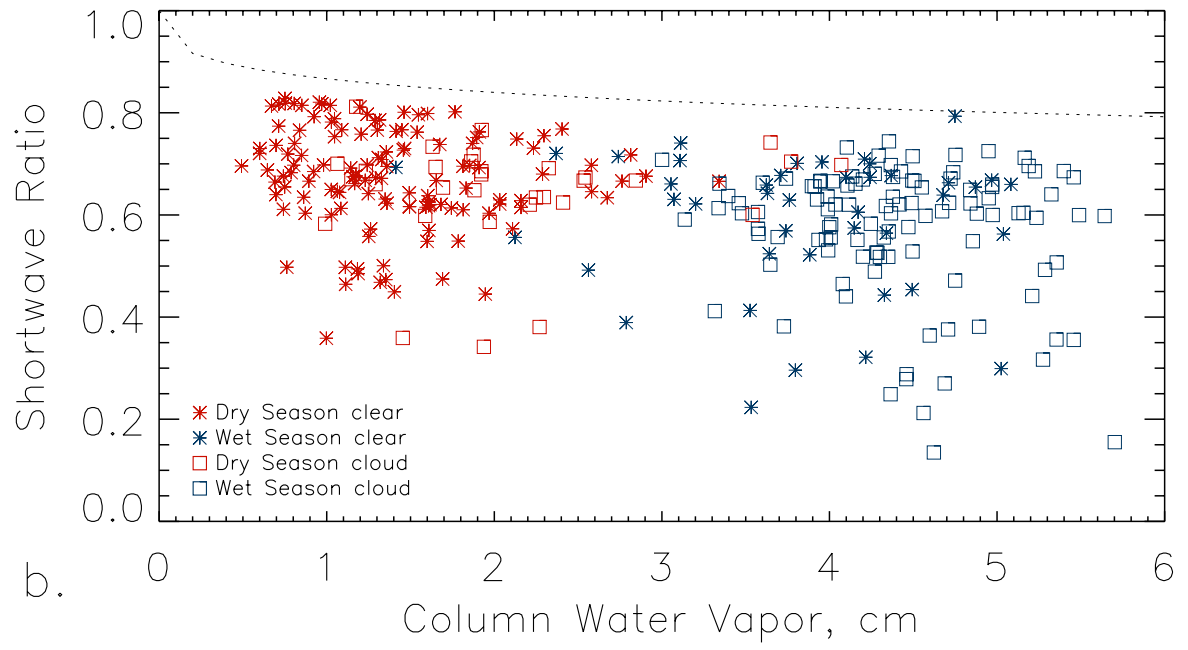


Figure 9

a.



b.

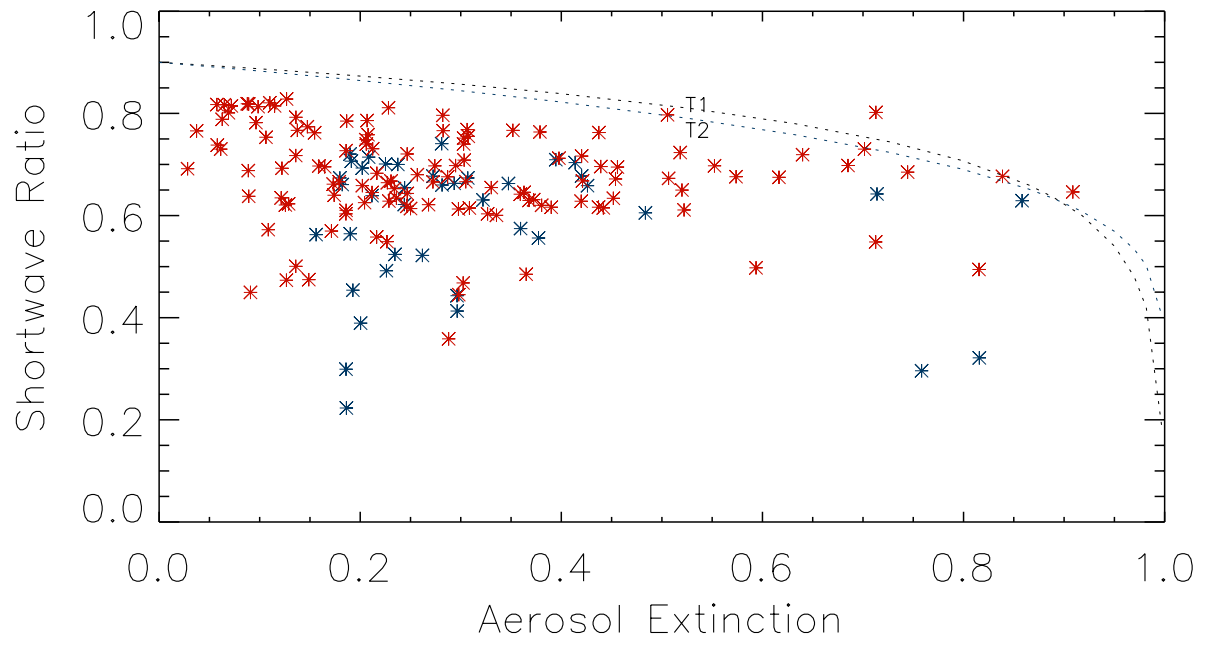
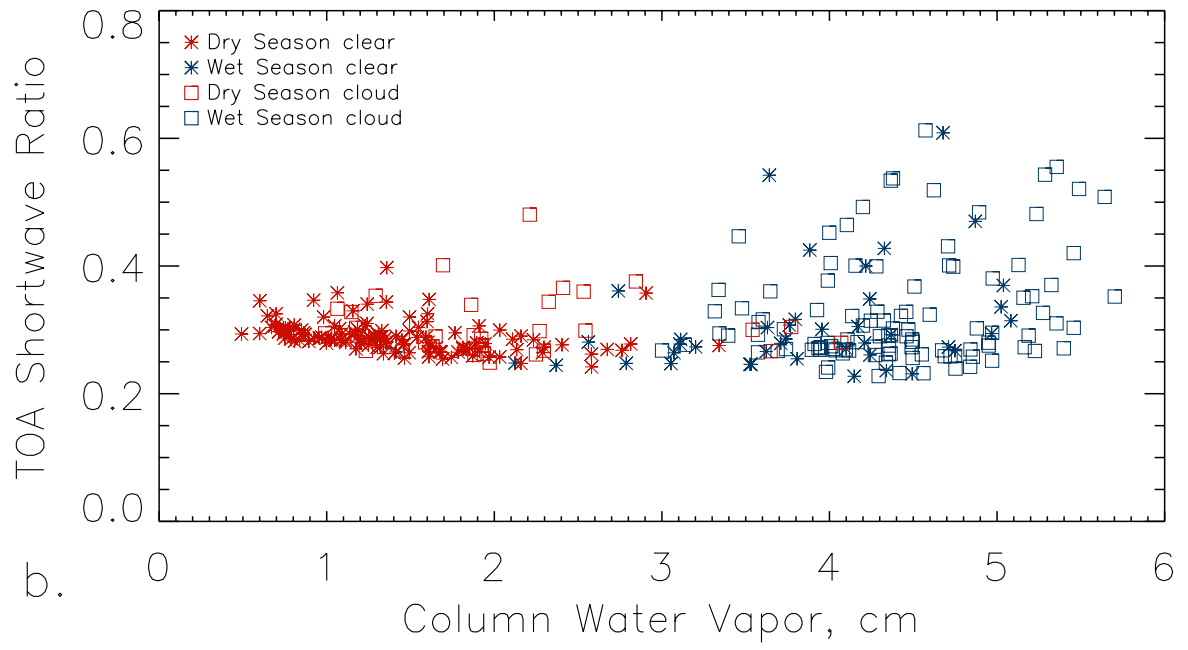


Figure 10

a.



b.

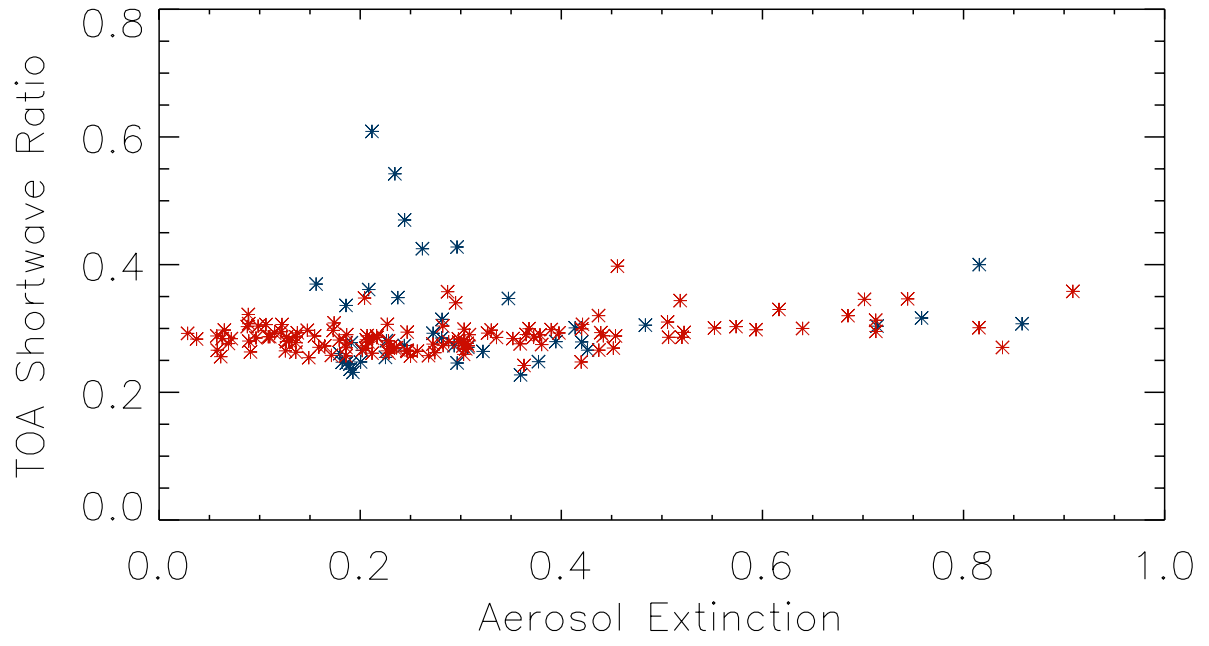


Figure 11

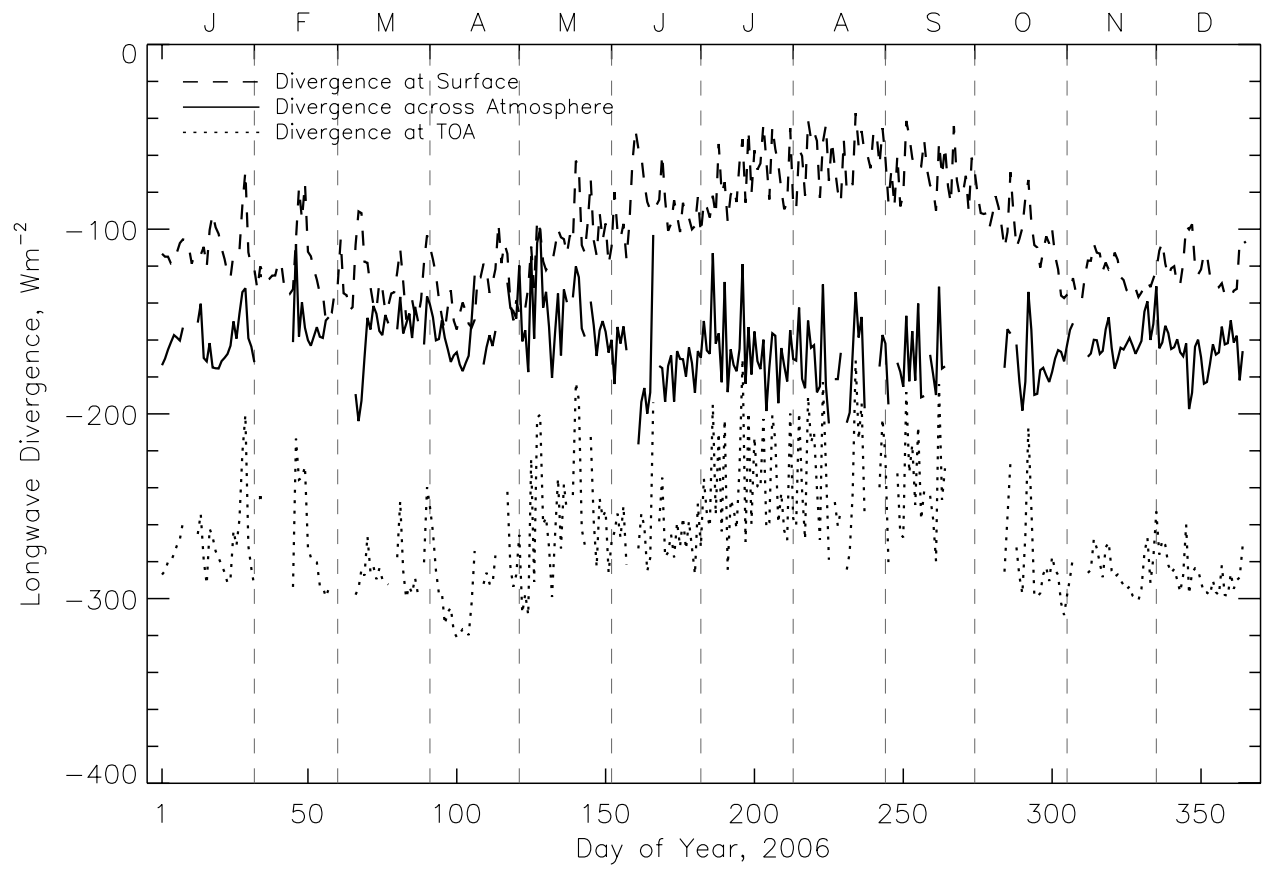


Figure 12

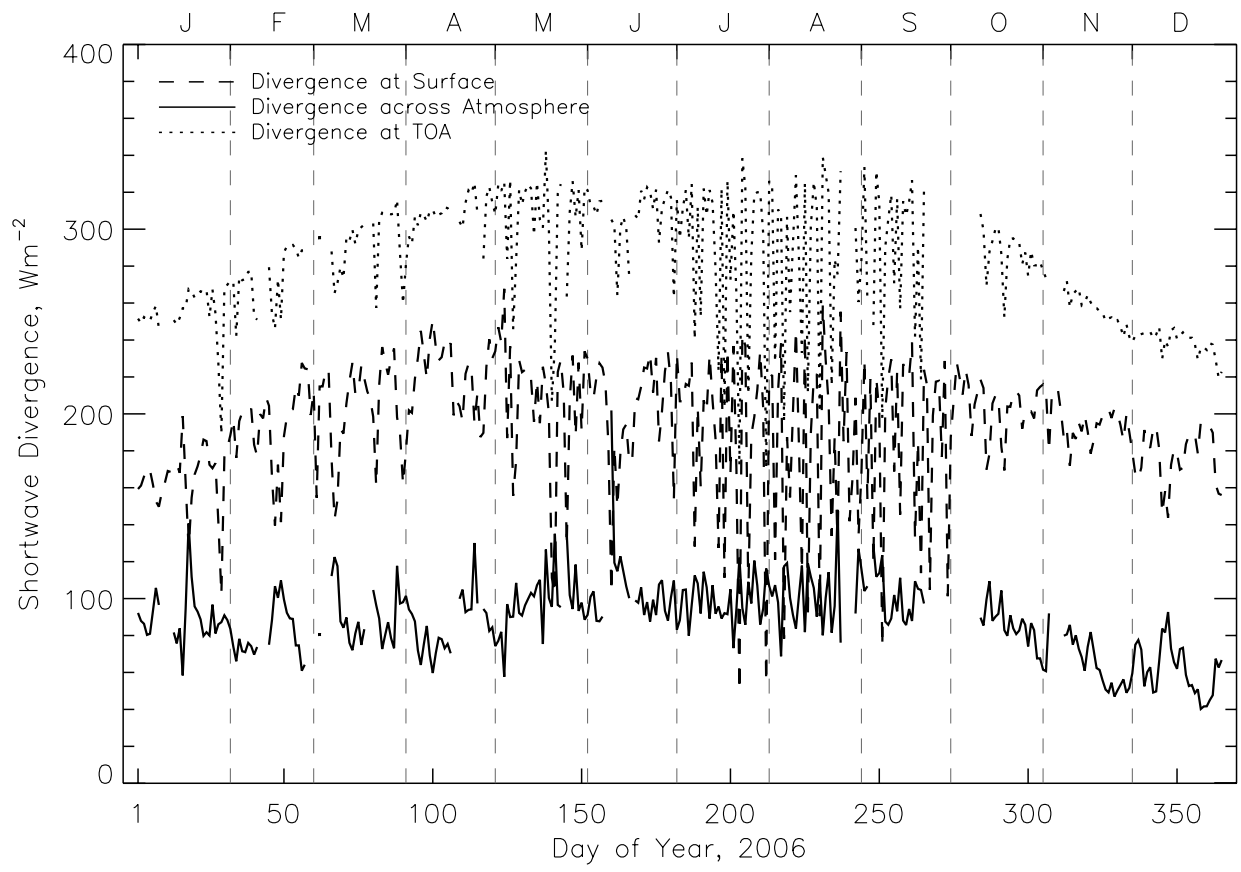


Figure 13

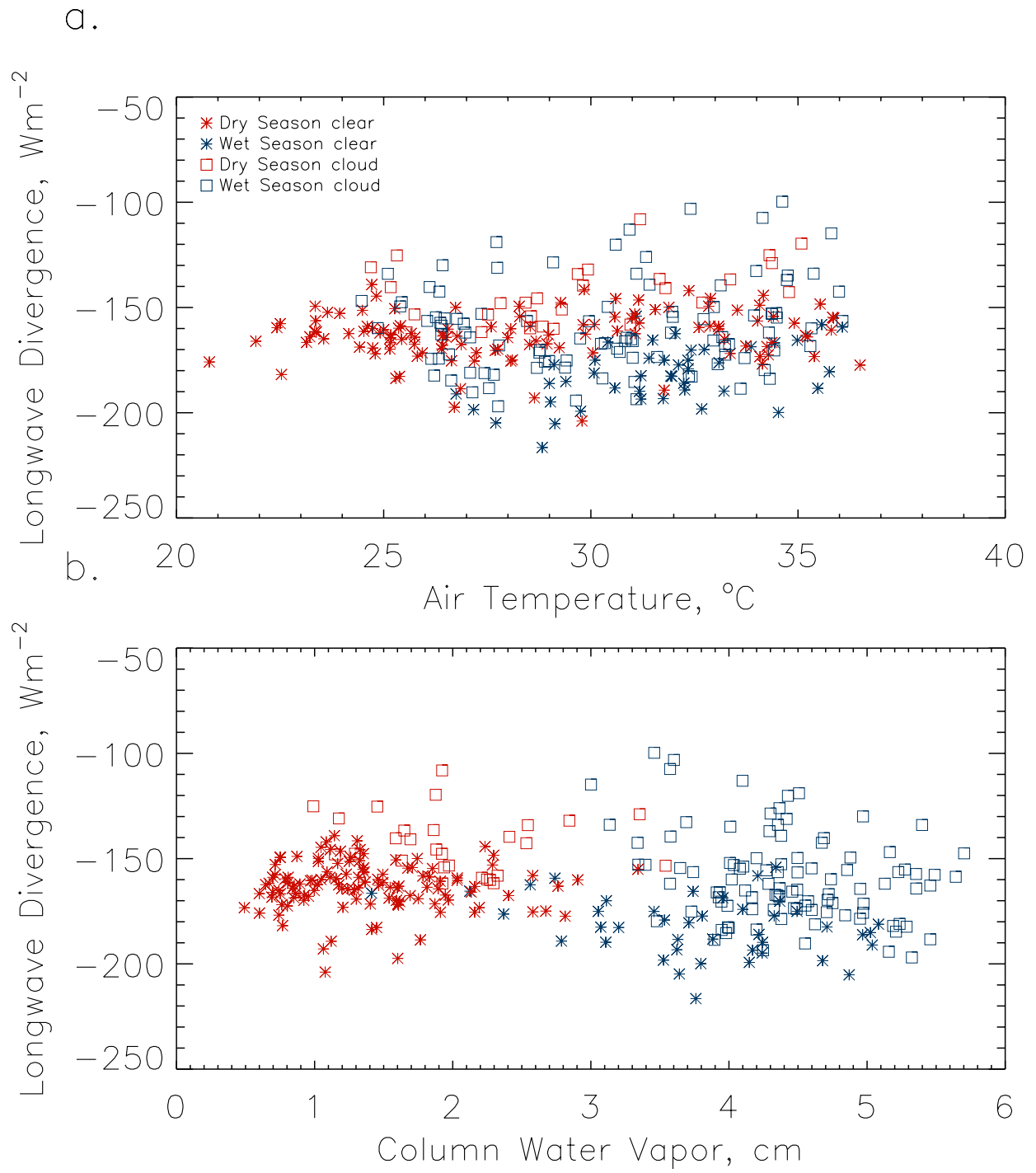


Figure 14

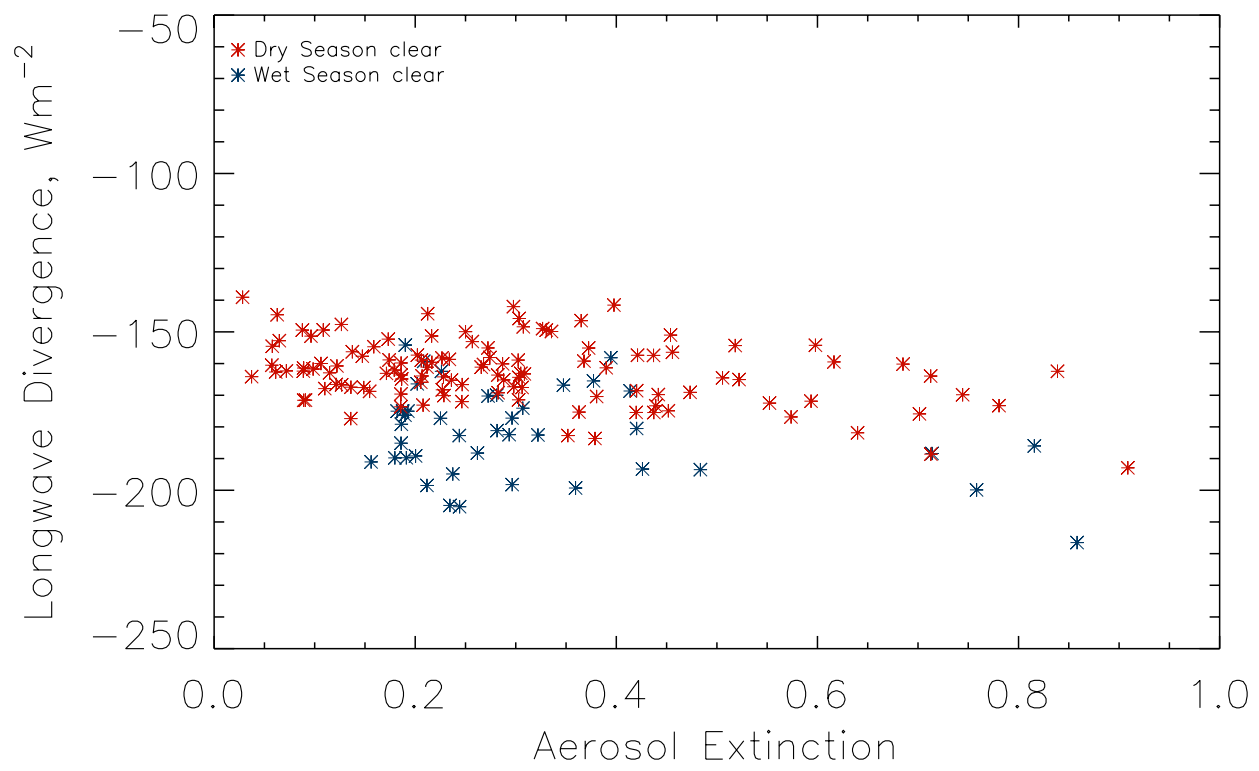


Figure 15

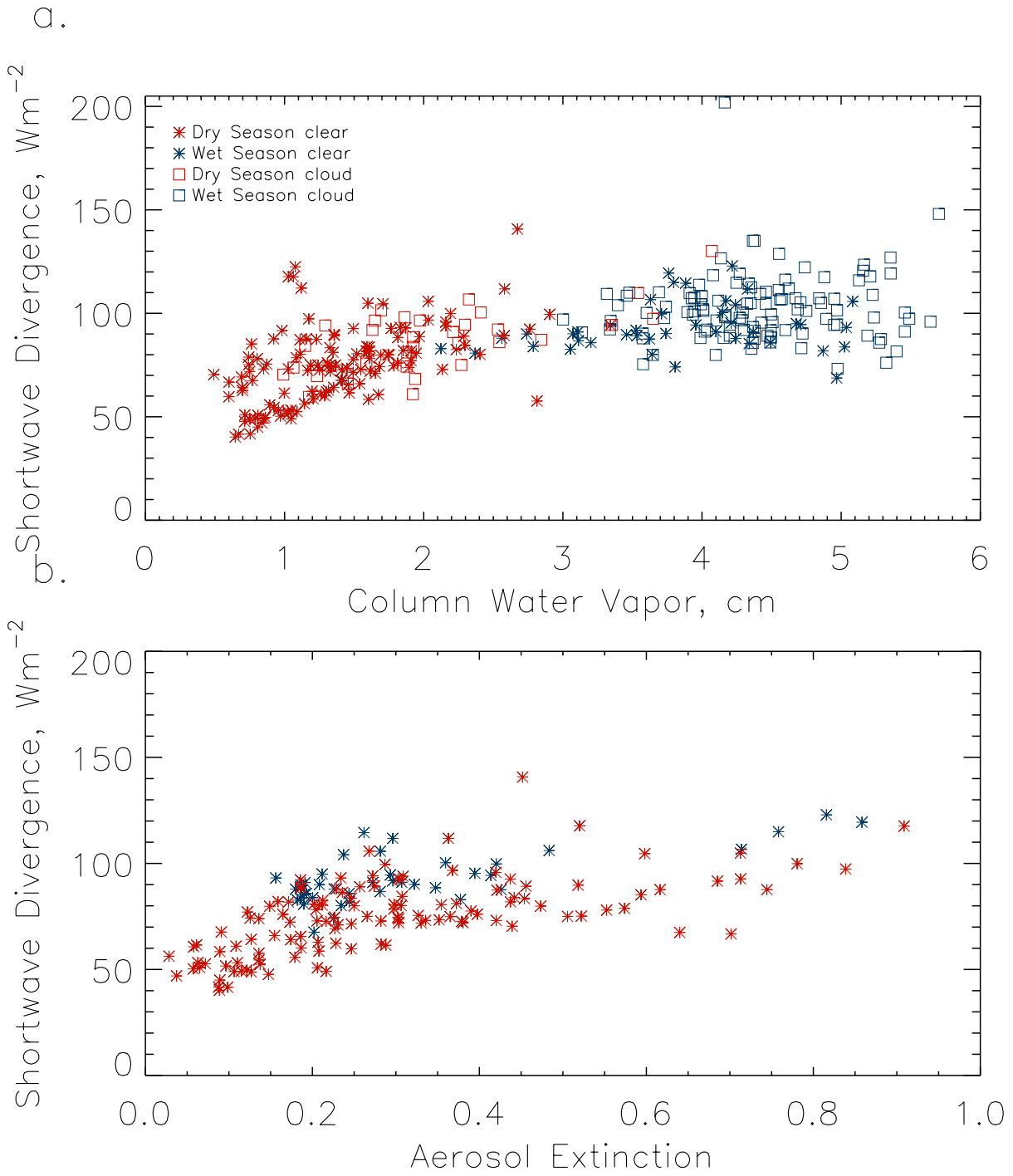


Figure 16

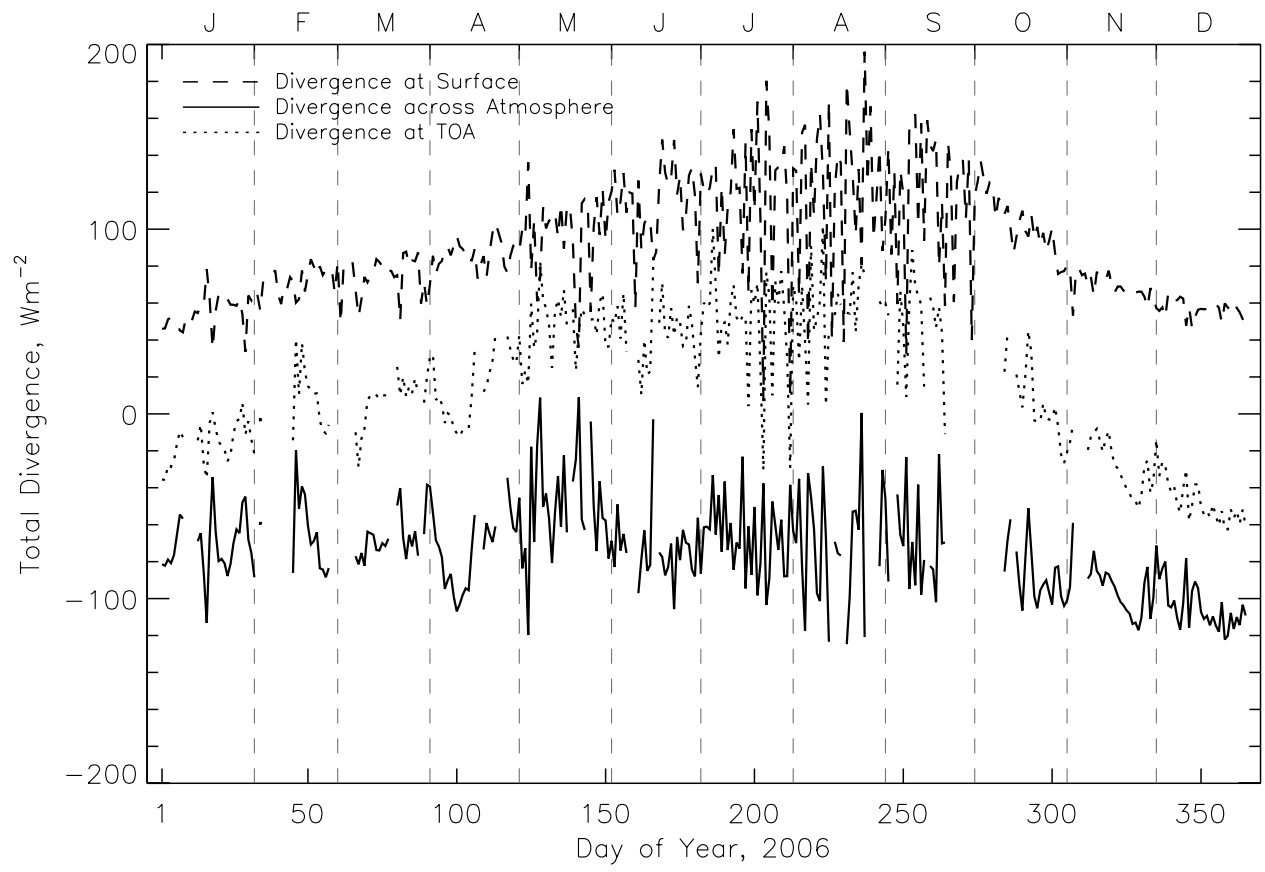


Figure 17

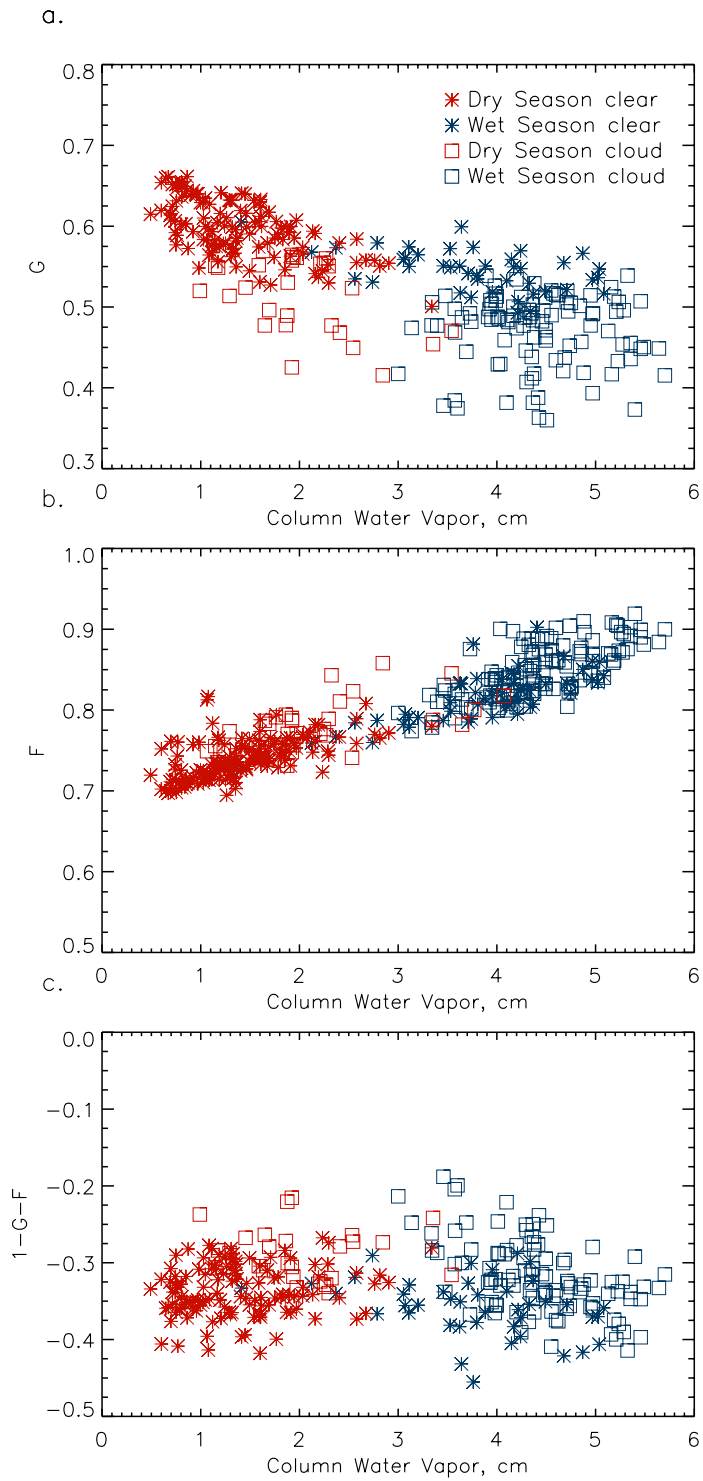


Figure 18

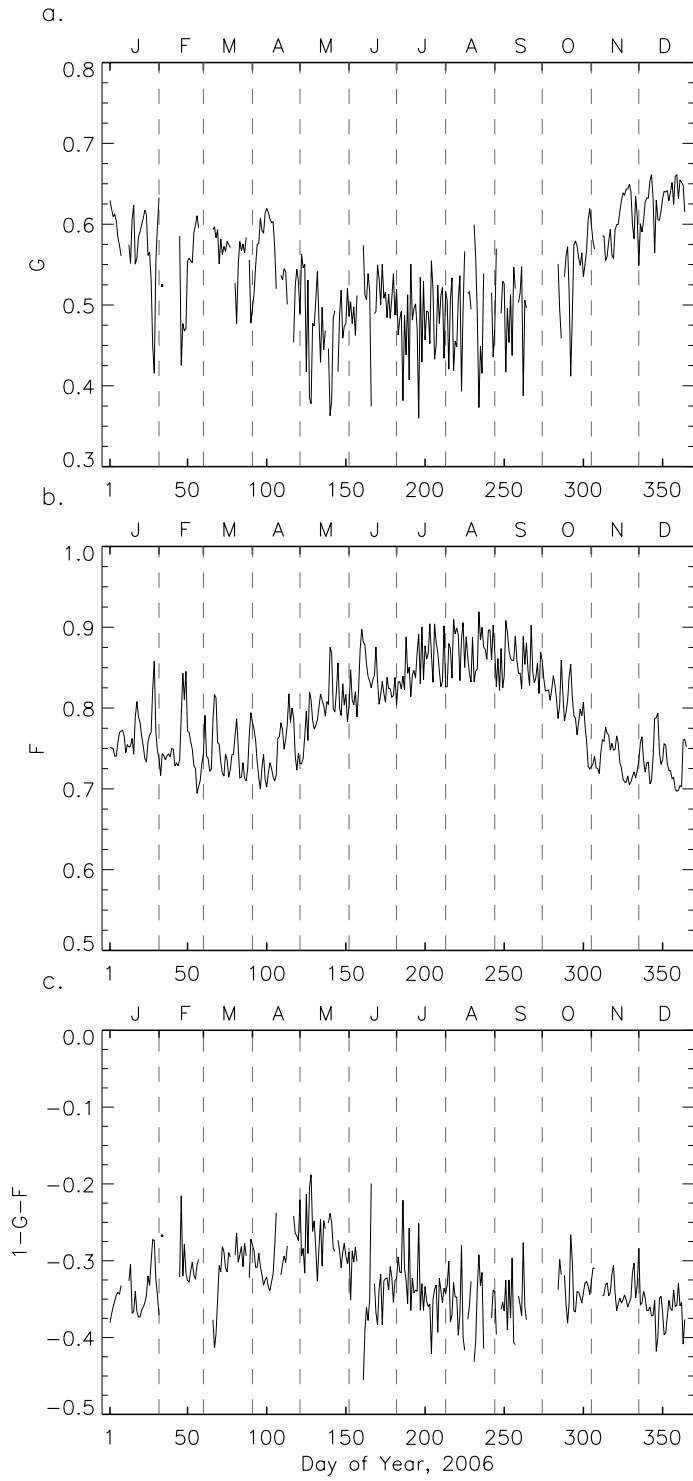


Figure 19